Available online at www.sciencedirect.com

ScienceDirect

Advances in Space Research 66 (2020) 2537–2555

ADVANCES IN SPACE RESEARCH (a COSPAR publication)

www.elsevier.com/locate/asr

First results from ITU-Dynasonde, Istanbul, Turkey on the ionospheric characteristics

Ayşegül Ceren Moral [a], Zerefşan Kaymaz [a,*], Emine Ceren Kalafatoglu Eyigüler [a], Nikolay Zabotin [b], Robert Livingston [c]

[a] İstanbul Technical University, Faculty of Aeronautics and Astronautics, Maslak, Istanbul, Turkey
[b] University of Colorado, Department of Electrical, Computer and Energy Engineering, Boulder, CO, USA
[c] Scion Associates, Port Townsend, WA, USA

Received 7 April 2020; received in revised form 23 August 2020; accepted 26 August 2020
Available online 17 September 2020

Abstract

Observations of the ionosphere over Istanbul, Turkey have been made using an ionosonde installed at the Istanbul Technical University (*ITU*) Maslak campus. In this paper, we present average diurnal, monthly, seasonal, and noon-midnight statistics of key *F2* layer parameters observed over a one-year period. Those parameters are the *F2* layer critical frequency (f_oF2), its peak height (h_mF2), and the estimated total electron content (*TEC*). The data show that the overall average behavior at Istanbul is consistent with the findings of other studies of the mid-latitude ionosphere. Also presented are the results of a close look at the diurnal variations of *F2* layer. Categorizing these variations provides suggestions about the possible causes or drivers that affect the Eurasian ionosphere.

Keywords: Dynasonde; Ionosphere; F2 layer critical frequency; Mid-latitudes; Ionospheric anomalies

1. Introduction

Accurate and timely space weather predictions of ionosphere require well understanding of the behavior of the ionospheric parameters such as critical frequency, peak electron density, peak height and TEC, their variations and their complex interactions with neutral atmosphere as well as magnetosphere and underlying physical and dynamical processes. The variations in these parameters can result from several sources and can be observed at different time scales. The sources include variations in the solar radiation flux, meteorological factors and solar and magnetospheric activity (Mendillo, 2006; Forbes et al., 2000; Prölss, 1995; Wright, 1962). While the solar radiation flux due to the variations in solar zenith angle drives diurnal, seasonal and annual variations (Ratovsky and Oinats, 2011; Titheridge and Buonsanto, 1983; Wright, 1962) in the electron density, the solar activity variations in EUV, X-Ray and hard X-ray wavelengths cause solar cycle variations on the orders of 27 days and 11 years (Ratovsky et al., 2009; Rishbeth and Mendillo, 2001). The meteorological factors such as the upward propagating gravity waves from the troposphere, tides, planetary waves and thermospheric neutral winds give rise to shorter variations ranging from tens of minutes to hours or days (Ratovsky et al., 2015; Song et al., 2013; Tsugawa et al., 2007; Bruinsma and Forbes, 2007; Hernández-Pajares et al., 2006; Tsugawa et al., 2004; Mendillo et al., 2002; Forbes et al., 2000; Rishbeth and Müller-Wodarg, 1999;

* Corresponding author.
E-mail addresses: moral@itu.edu.tr (A.C. Moral), zerefsan@itu.edu.tr (Z. Kaymaz), ceren.kalafatoglu@itu.edu.tr (E.C. Kalafatoglu Eyigüler), nikolay.zabotin@colorado.edu (N. Zabotin), livingston@scion-associates.com (R. Livingston).

https://doi.org/10.1016/j.asr.2020.08.034
0273-1177/

Rishbeth, 1998; Fuller-Rowell et al., 1994). Magnetospheric disturbances caused by magnetic storms and magnetospheric substorms that occur in response to solar activity also drive variations in the ionospheric density on the order of minutes to hours such as TIDs (Cherniak and Zakharenlova, 2018; Kim and Hegai, 2009; Borries et al., 2009; Richmond and Lu, 2000; Kirchengast, 1997; Fuller-Rowell et al., 1996, 2000; Francis, 1974; Torr and Torr, 1973).

Large scale statistical behavior of the ionosphere at different latitudes has been well characterized in several studies. Among these, Zou et al. (2000) classified the features seen in electron density variations at mid-latitudes in three groups as: (1) winter (or Seasonal) anomaly, (2) semi-annual (equinoctial) anomaly, and (3) annual anomaly. Winter anomaly describes the case when noon electron density in winter (December) is greater than noon electron density in summer (June) while semi-annual anomaly refers to the case when equinox electron densities at noon are greater than those of solstice. In contrast to semi-annual anomaly, the annual anomaly occurs when the worldwide summer (June) electron densities both at noon and midnight are consistently lower than those of the worldwide winter (December) at noon and midnight. The winter anomaly was found to be less pronounced at lower latitudes and increased toward high latitudes as well as enhanced with the rising solar activity (Lee et al., 2011; Park et al., 2010; Zou et al., 2000; Rees, 1995; Torr and Torr, 1973; Wright, 1962). It was also shown that the winter anomaly becomes more intense with the increasing geomagnetic activity (Yasyukevich et al., 2018) and limited to auroral regions where magnetic disturbances exist during low solar activity (Torr and Torr, 1973). In contrast, at night, no winter anomaly was observed meaning that nighttime electron densities are smaller in winter than in summer at all latitudes (Zou et al., 2000; Wright, 1962). The peak of the maximum electron density in winter was shifted from post noon at mid-latitudes to afternoon at high latitudes while at low latitudes, it was seen centered around noon independent of seasons. The minimum in electron density, on the other hand, was obtained in December at pre-dawn around 05:00 am at all latitudes. Both the TEC below F2 peak and h_mF2 don't exhibit any winter anomaly (Wright, 1962).

Most of these studies invoke thermospheric response to the solar radiation input to explain the winter anomaly at mid-latitudes (Lee et al., 2011; Zou et al., 2000; Fuller-Rowell et al., 1994, 1996). Rishbeth and Mendillo (2001) provide a more complete summary of possible processes. The variations in solar radiation input change the neutral composition and temperature of the thermosphere which in turn affect the rate of ion-electron recombination rate (Rees, 1995; Fuller-Rowell et al., 1994, 1996; Wright, 1962). Increased thermospheric temperatures result in higher electron loss rates compared to the production rates at F region altitudes during the daytime in summer season at all latitudes (Zou et al., 2000; Fuller-Rowell et al., 1994; Wright, 1962). In addition, magnetospheric substorms create electric fields and waves at the ionospheric heights which in turn give rise to changes in the thermospheric neutral winds and the neutral composition as well (Fuller-Rowell et al., 2000; Mendillo, 2006; Prölss, 1995, 2006). Thermospheric neutral winds can remove electrons from one region by moving those along the magnetic field lines to different altitudes (Fuller-Rowell et al., 2000; Zou et al., 2000; Rishbeth et al., 2000). Winter anomaly is generally attributed to the seasonal changes in the chemical composition of the thermospheric neutral air, especially in the ratio of atomic oxygen to atomic nitrogen (Rishbeth 1998; Rishbeth and Mendillo, 2001; Wright, 1962; Rishbeth and Setty, 1961). Duncan (1956) invoked compositional changes produced by the global summer-winter thermospheric circulation. These studies were verified by the global modelling studies such as in Fuller-Rowell and Rees (1983). The peak electron densities during magnetically active times can both decrease and increase with respect to a quiet day background (e.g. Mendillo, 2006). While solar heating creates daily variations in consistent with the Chapman law during the day at low latitudes, it becomes less and less consistent with Chapman law toward mid- and high latitudes where the winter anomaly is seen predominantly. Auroral heating was suggested to be insufficient to create a variation consistent with Chapman Law during the day in winter at high latitudes (Yasyukevich et al., 2018; Rishbeth and Mendillo, 2001; Wright, 1962).

In addition to winter anomaly, several studies exhibited the existence of semi-annual anomaly at low latitudes (Wright, 1962), mid- and high latitudes (Wright, 1962; Zou et al., 2000; Park et al., 2010; Torr and Torr, 1973; Torr et al., 1981). The presence of semi-annual variations was linked to semi-annual variations in neutral density (Fuller-Rowell, 1998; Rishbeth and Müller-Wodarg, 1999), semi-annual variation in geomagnetic activity known as the Russell-McPherron effect (Russell and McPherron, 1973; Waltersheid, 1982), external forcing of the upper atmosphere by the solar wind (Lal, 1992, 1998; Zhao et al., 2007; Verkhoglyadova et al., 2013). Zou et al. (2000) considered solar driven photochemical and dynamical processes within the thermosphere itself and contributions auroral precipitation to explain the semi-annual anomaly in their data. While Park et al. (2010) found increased semi-annual activity at mid-latitude Japan as solar activity increases, Torr and Torr (1973) reported a decreasing semi-annual component at mid-latitudes with decreasing solar activity. Park et al. (2010) attributed the presence of semi-annual anomaly to the Russell McPherron effect. Larger southward $IMF\ B_z$ during equinoxes drives more and stronger geomagnetic storms. Therefore, ionospheric electron density during equinoxes increases as a result of the particle precipitation from the magnetosphere when the solar activity is high. Torr and Torr (1973) and Torr et al. (1981), on the other hand, ascribed the equinoctial variations in their data to the semi-annual

variations of neutral densities associated with the geomagnetic and auroral activity.

These early studies have shown that even the mid-latitude ionosphere is shaped at various time scales, by the complex interactions of plasma production, geomagnetic drivers, and thermospheric neutral dynamics. Many of these studies utilized ionosonde data which was the motivation to install the ionosonde at ITU in order to study the ionospheric variations over Istanbul. While these previous studies provide a global perspective within which to view ionospheric behavior in the Eurasian sector, it has not been studied in detail. Our aim in this study is to investigate the typical characteristics of ionosphere over İstanbul by using the high resolution measurements of *TEC*, critical frequency (f_oF2), peak height (h_{max}) from ITU-Dynasonde. We describe the features that characterize the ionospheric behavior using high resolution data, compare with those in the literature and address on the possible causes. Such high resolution observations, at various spatial and temporal scales, will help to reveal and understand the underlying physical processes that are active in our sector. The paper is organized as follows: Section 2 and Section 3 present the instrumentation and results respectively. While Section 4 discusses and compares our findings with those in the literature, Section 5 summarizes and concludes the study.

2. Instrumentation and data

In this study, we use the Istanbul Technical University (*ITU*) Dynasonde radar system which is a combination of an advanced *HF* radar built by Scion Associates, Inc. (often referred as *VIPIR*, Vertical Incidence Pulse Ionospheric radar) and a Dynasonde Software Suite (developed at the University of Colorado Boulder) to diagnose the ionospheric conditions. A history of Dynasonde, Dynasonde tutorial and a list of associated papers (https://www.ngdc.noaa.gov/stp/IONO/Dynasonde/) provide a comprehensive summary on the software and hardware developments leading to today's Dynasonde system. There are currently *11* Dynasonde stations working actively over the world. Hardware part of the *ITU* Dynasonde has *1* transmitter, *4* receivers, a transmitting (inverse delta design) antenna, and *4* receiving dipole antennas. Transmitting antenna is supported by a *25 m* high tower and it sends *HF* pulses almost omnidirectionally in the frequency range from *0.1* to *25 MHz*. Four receiving antennas, each supported with *5 m* high poles, are located very close to the transmitting antenna to accomplish a monostatic mode of operation. The system operates the Dynasonde Software Suite *2012* (Wright and Zabotin, 2005; Zabotin et al., 2005) for the data analysis. Advanced inversion procedure, *NeXtYZ* (Zabotin et al., 2006), provides *3-D* dimensional distribution of the echo locations using phase-based methods in each ionogram and drives true height electron density profiles from the virtual height data using modern ray tracing techniques in a Wedge Stratified Ionosphere (*WSI*). These features constitute a great advantage when compared to its precedents such as *POLAN* (Titheridge, 1985), and *NhPC* (part of the Digisonde data processing system *ARTIST*) (Reinisch and Huang, 1983) that both use approximation of plane horizontal ionospheric sheets. *NeXtYZ* provides information on true height electron density profiles from *70 km* to *800 km*. The main part of this information is extracted from the phase-based parameters of numerous *HF* echoes, and another part represents analytical empirical models of the underlying ionization and the *E-F* valley developed by J. Titheridge (Titheridge, 2000, 2001, 2003a, 2003b) that are appropriately fitted to the actual data. Topside part of the ionogram above the *F*-region peak has been obtained by extrapolating the electron density near the *F*-region peak according to Chapman law (Wright, 1960a, 1960b). The three parameters of the Chapman model are calculated based on fitting this model to many (several tens) data points obtained from ionospheric echoes for the region just below and close to the layer peak. The detailed information on Dynasonde technique and on the derivation of the electron density profile by *NeXtYZ* can be found in (Zabotin et al., 2017; Rietveld et al. 2008; Zabotin et al., 2006; Zabotin et al., 2005; Wright and Pitteway, 1996, 1999).

NeXtYZ was tested in real-time and compared with POLAN and Digisonde *NhPC* as well as with the simulated data. It was found that it is more robust and uniform against pitfalls of bad and insufficient data, trace selection and satisfactory in error predictions (Zabotin et al., 2006). The Dynasonde analysis output was also compared with *EISCAT* incoherent radar data and found that the vector velocities produced by Dynasonde echoes showed good agreement with *EISCAT* plasma data (Sedgemore et al., 1996, 1998). Dynasonde products were used to study a variety of scientific phenomena such as wave activity in the thermosphere-ionosphere system (Zabotin et al., 2017), atmospheric gravity waves (Negrea et al., 2016, 2018), thermospheric tides (Zabotin et al., 2017), TIDs, polar mesospheric summer echoes (Liu et al., 2002), artificial aurora experiments based on statistical data sets obtained from Tromso Dynasonde (Tsuda et al., 2018), ionospheric tomography (*TEC*, f_oF2) using two Antarctica Dynasondes (Heaton et al., 1996), local ionospheric variations over the Chund Li Dynasonde in Taiwan (Hsiao et al., 2008), dynamic properties of the ionosphere over Antarctic Jang Bogo station (Ham et al., 2000; Kim et al., 2018), etc. Each of these studies indicated the success of the Dynasonde software and its products in studying the physical and dynamical problems of the ionosphere at different locations and different time scales.

The Dynasonde radar system was installed in Istanbul (geographic 41^oN, 29^oE, geomagnetic 39^oN, 108^oE) in September *2012* and the continuous data at *4* min resolution started to stream from October *2012*. The instrument is located within the Maslak Campus of the Istanbul Technical University in the region of Sarıyer, near the Bos-

phrous. Panels *a, b, c, d* and *e* in Fig. 1 illustrate the instrument site location, the transmitting antenna, one of the four dipole receive antennas, and the radar rack.

In this study, we analyze the critical frequency (f_oF2), peak height (h_mF2), and Total Electron Content (TEC) data covering the period from October *2012* to September *2013* in Section 3.1 and from October *2012* to November *2014* in Section 3.2. Fig. 2 presents two examples of the Dynasonde ionogram display, one recorded in April *21, 2013* at *09:00 UT* (*11:00 LT*) close to local noon (top panel), and another at *21:00 UT* (*23:00 LT*) close to midnight (bottom panel). The Local Time (LT) is defined as $LT = UT + 2\ h$ for İstanbul.

The horizontal axis in Fig. 2 is the plasma frequency (for the profile) and the radio frequency (for the echoes) varying from *1.5 MHz* to *16 MHz* and the vertical axis gives the virtual range (for the echoes) and the true height (for the profiles) in *km*. The colored dots represent individual ionospheric radio echoes grouped by the analysis code into traces according to their physical properties and their association with specific ionospheric structures (*E*-region, *F*-region, sporadic *E*, *O*- and *X*- traces). Echo recognition and their selection are explained in detail in the references above. Briefly, characteristics of each echo that corresponds to a specific radio frequency are compared to the average characteristics of those echoes already selected before it is included in a trace or rejected. Traces are the dynamic classes or the groups of echoes that are physically meaningful and can be selected for the further inversion analysis steps or rejected altogether. The numbers in the ionogram images relate to the traces, not to the echoes. The trace number is placed in the image a little below and to the right from the average position of all the echoes in the trace. The "*" sign with an enumeration indicates traces selected by the software for the inversion purposes, and the "<" sign with an enumeration indicates those rejected for the inversion purposes (i.e. *Z*-traces, sporadic *E* traces, and multiple reflections (Zabotin et al., 2006). The color and the enumeration of the traces do not have any physical meaning by themselves. These may differ from one ionogram to another. Both ordinary mode and extraordinary mode traces are observed and used for the inversion (Zabotin et al., 2006). The thin, solid red line represents the true height electron density profile, one of the basic results of the inversion. Its portion with the error bars is the one actually inverted from the phase-based parameters of numerous *HF* echoes, and the one without the error bars represents analytical empirical models of the underlying ionization and the *E-F* valley appropriately fitted to the actual data. The contribution of the topside part of the profile in total electron density is estimated according to the Chapman model (Zabotin et al., 2006). The inserts show the background radio noise level, the returned signal strengths, and an estimate of the tilt of the ionosphere. Figure displays noon and midnight differences in electron density clearly with f_oF2 at *8 MHz* and *5 MHz* at *290 km* and *320 km* respectively. *E* region is also apparent in daytime ionogram at about *110 km*. Since we make emphasis on *F* region characteristics in this paper, *E*-region study is deferred to another study. We note that even though the year of *2013*, the year that includes our data range, corresponds to the peak time of the solar activity period, the day of April *21, 2013* was a magnetically quiet day with no solar or magnetospheric activity recorded on Earth.

3. Results

3.1. Diurnal, monthly and seasonal variations

Fig. 3 illustrates time series plots for f_oF2, h_mF2, and TEC corresponding to the day when the ionograms in Fig. 2 were extracted from. The panels from top to bottom are (a) critical frequency, f_oF2, (b) peak height, h_mF2, and (c) Total Electron Content, TEC, in $TECU$ where *1*

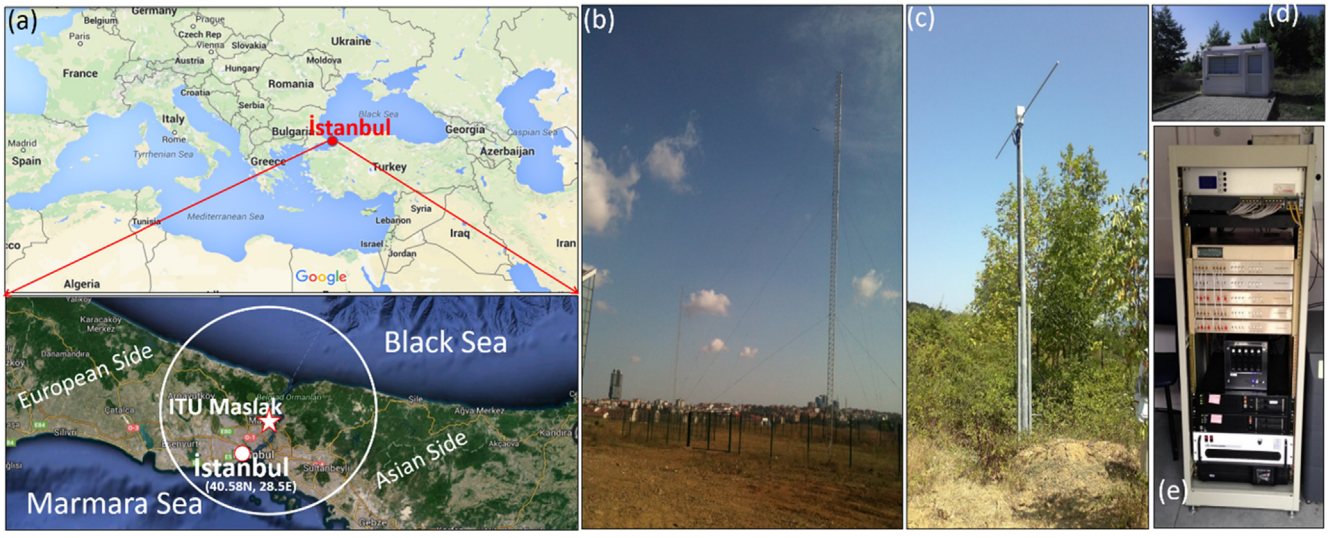

Fig. 1. (a) Location of the experiment site in Istanbul, Turkey (*40.58°N, 28.5°E*), (b) Transmitter, (c) Receiver, (d) Shelter and (e) Radar. (For interpretation of the references to color in this figure legend, the reader is referred to the web version of this article.)

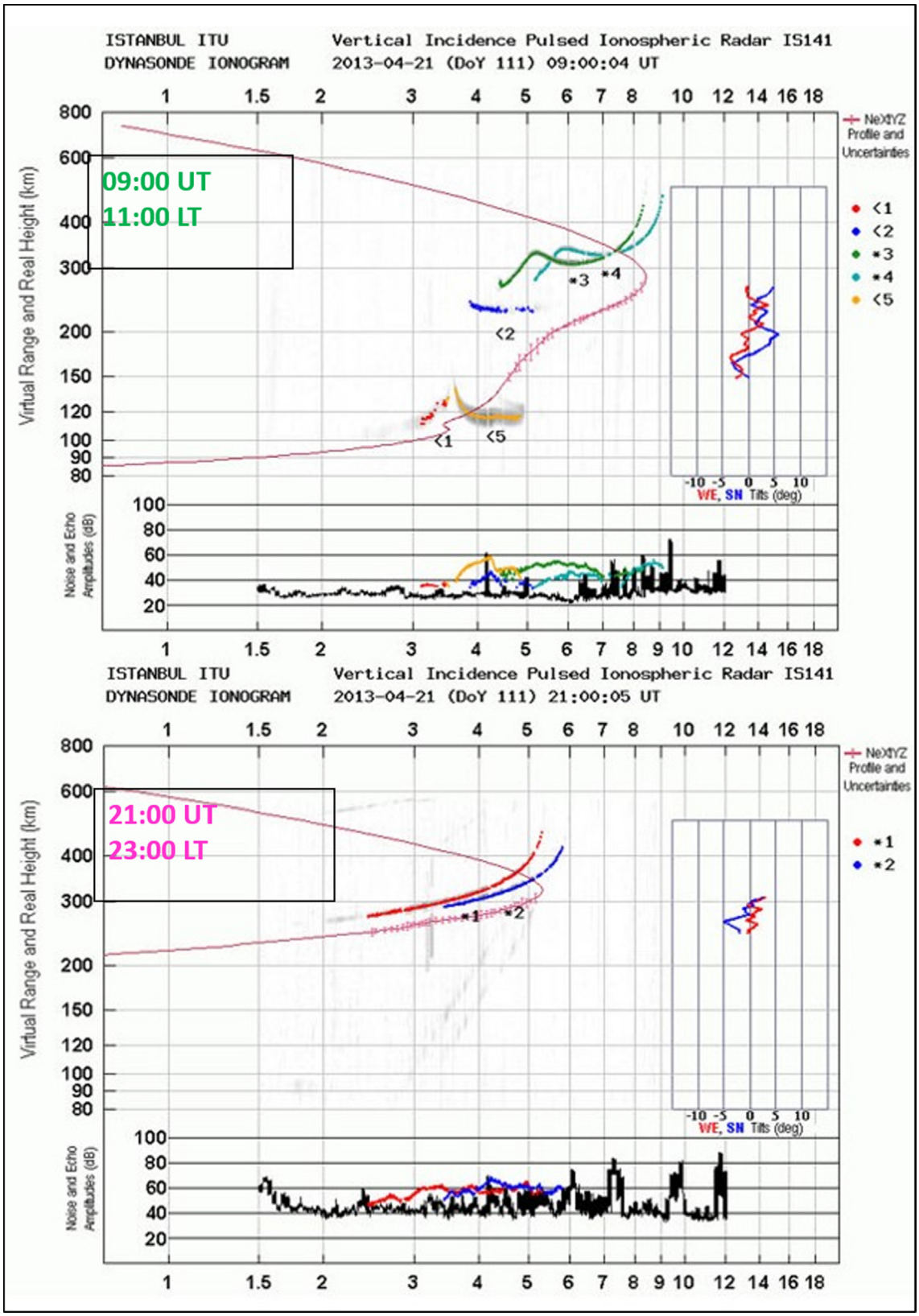

Fig. 2. An example of ionogram on April *21, 2013* showing the electron density variation with true height at *09:00 UT (11:00 LT)* (top), and *21:00 UT (23:00 LT)* (bottom). (For interpretation of the references to color in this figure legend, the reader is referred to the web version of this article.)

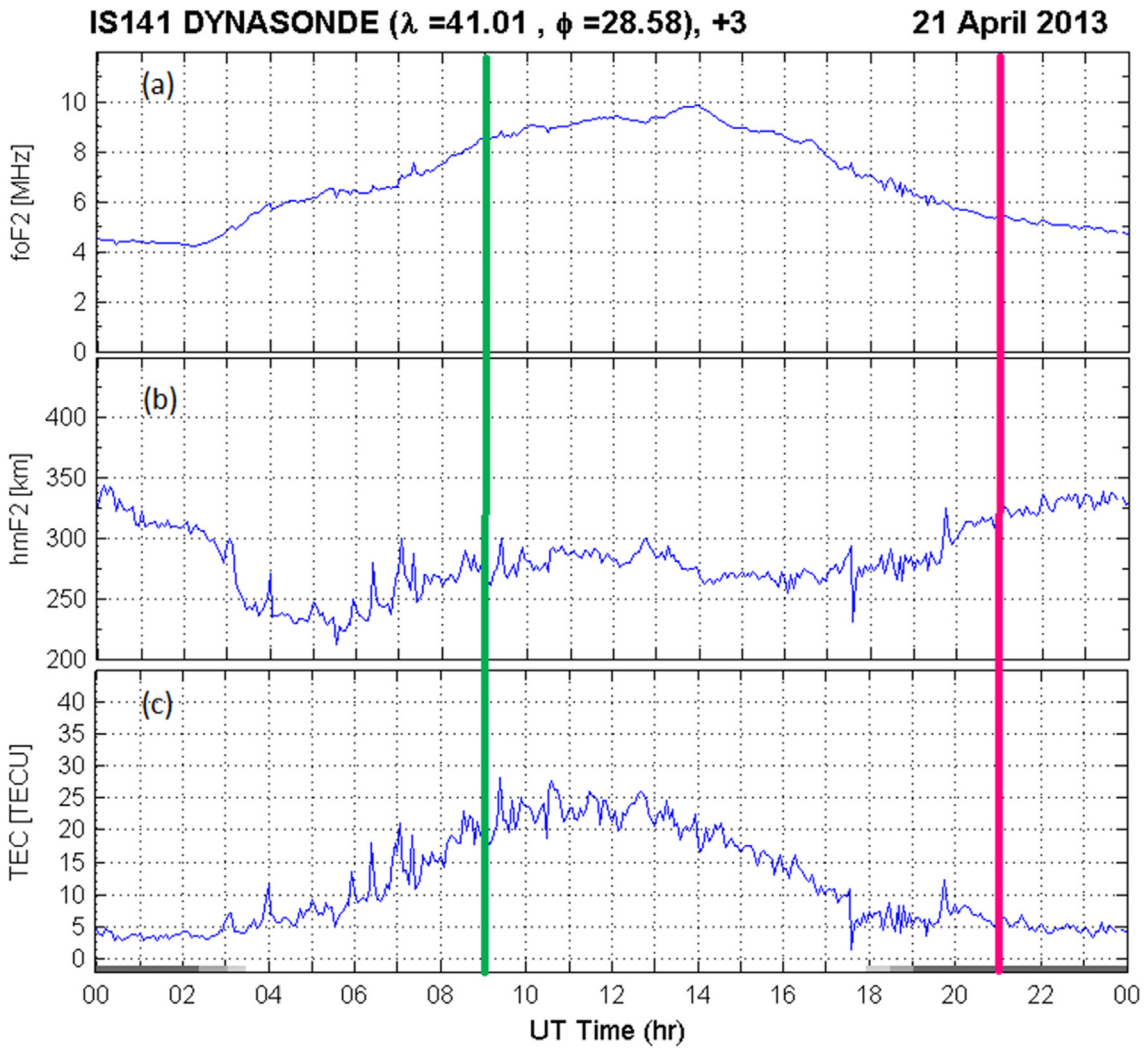

Fig. 3. Time series plots of (a) critical frequency (f_oF2), (b) peak height (h_mF2), and (c) Total Electron Content (*TEC*) on April *21, 2013*. The time on the horizontal axis is given in *UT*. Green and pink vertical lines at *09:00 UT* and *21:00 UT* correspond to the times when ionograms in Fig. 2 are extracted. Black and gray shades at the bottom of Panel *c* show the daylight extent for the day. (For interpretation of the references to color in this figure legend, the reader is referred to the web version of this article.)

$TECU = 1 \times 10^{16}\ m^{-2}$. Here we note that the *TEC* in Panel *c* is the integrated vertical electron density obtained from the true height profile from *70* to *800 km* as described above (Zabotin et al. 2006). Time on the horizontal axis is given in *UT* from *00:00 to 24:00*. The vertical lines mark the times when those ionograms in Fig. 2 are taken at *09:00 UT* and *21:00 UT*. The daylight duration is also added in black and gray colors at the bottom of Panel *c*.

Throughout the paper, we used the critical frequency (f_oF2) to refer to the peak electron density (N_mF2) as they are related to via $N_m = 1.23 \times 10^4 f_o^2$ where f_o is f_oF2 in *MHz* and N_m is N_mF2 in cm^{-3}. Since Fig. 3 represents an example of a single day for the statistics presented in this paper, we explain the features seen in this figure in some detail. Panels *a* to *c* in Fig. 3 display a typical diurnal variation of f_oF2, h_mF2 and *TEC* over our station on this day. f_oF2 appears to follow variations in the solar zenith angle with a midday maximum and midnight minimum described by Chapman law. In the figure, it varies from a minimum of about *4 MHz* during night time to about *10 MHz* at the peak that occurs around *14 UT (16:00 LT)*. At local noontime (*12:00 LT*), it is about *9 MHz*. *TEC* in Panel-c shows a similar diurnal variation as well which is consistent with the solar zenith angle. The peak occurs at *13:30 LT*, i.e. *1.5 hrs* later than the local noon at *12:00 LT*. It is seen to be around *5 TECU* throughout the night time and starts increasing at *06:00 LT*. The peak value is seen to be *24 TECU*. It is clear that both f_oF2 and *TEC* peaks occur sometime later than the local noon being *4 hrs* and *1.5 hrs* later than the local noon respectively. The peak in f_oF2 occurs *2.5 hrs* later than the peak in *TEC*. It appears that ionospheric dynamics produce a *TEC* variation closer to the Chapman theory than f_oF2 is. Here, we note that similar delays with respect to noon time in total electron content below *F* peak were reported in Wright (1962).

Another feature emerging in *TEC* plot on this day is the fluctuations which are present during the daytime and to a lesser extent during the nighttime as well. Scanning through single day plots of *TEC* in summer and winter indicates that TEC exhibits more fluctuations than f_oF2 does. This is also the case seen in f_oF2 plot of Panel *a* in Fig. 2. *TEC* illustrates more fluctuating structure while f_oF2 presents rather smooth, gentle variations during the day. *TEC* fluctuations of such kind observed almost every day, especially, during the summer months suggest highly dynamic ionosphere over our station. Fig. 3 exposes these fluctuations on the order of *4* min, which is the resolution of the data, on this day of the year. Such fluctuations superimposed on the background diurnal electron density are seen to be one of the typical characteristics of the summer ionosphere over this region.

Panel *b* in Fig. 3 presents the variations in the real ionospheric height, h_mF2. The h_mF2 fluctuates all day but less from noon to evening. It varies from a minimum *210 km* at *06:00 LT* to a maximum of *350 km* at midnight. At local noon time, it is about *290 km*. The midnight ionosphere, thus, is seen to be higher about *60 km* than the noontime ionosphere on this day. Two minima characterize h_mF2 variations during the day: one occurs at about sunrise, *06:00 LT,* as *210 km*, and the other is at about sunset, *18:00 LT* as *280 km*. A distinct feature seen in all scanned daily time series of h_mF2 is that the ionosphere is always higher at sunset than at sunrise over our station.

Fig. 4 provides an illustration for the monthly averaged diurnal variations of f_oF2. The figure was created by taking average of f_oF2 data at each *4* min in each day over the entire month. The month and the year are indicated at the top, left corner in each panel. The time span for this figure covers one year from October *2012* to September *2013*. The horizontal and vertical axes show the time of the day and monthly averaged f_oF2. The columns from left to right comprise the months in each season in the order of autumn, winter, spring and summer. The figure illustrates both diurnal f_oF2 variations averaged over the month but also variations from month to month. In the figure, it is immediately possible to notice that the summer months show strong fluctuations compared to the winter months implying a dynamic and active ionosphere in summer. Months with smoother variations and less fluctuations, on the other hand, indicate a quiet or less dynamic ionosphere. Averaging of each *4* min f_oF2 over a month will smooth out some of the variations resulting from single events in a day but will not remove those with large amplitudes or those that may occur recursively during a month. We attribute the differences between the fluctuation levels in summer and winter to the dynamic nature of the ionosphere and find that it is one of most characteristic features of the electron density structure in this region. In addition, the summer months show broader noon time peaks extending over several hours, and not as pointy as in the winter months. Also, the peak f_oF2 is much lower at noontime in summer months than it is in winter months. This indicates a reduction of electron density at noon time during summer months. This may be a result of the neutral winds that uplift electrons along the magnetic field lines, thus removing electrons from F-region heights to a different altitude in summer. As a consequence, the difference between noon and midnight f_oF2 in summer months becomes smaller compared to that in winter months. On average, the noontime f_oF2 is found to be greater than 8 *MHz* from September till June, and the highest in October at about *11 MHz*, while it varies between *6 MHz and 8 MHz* from June till September, being the highest in June. On the other hand, midnight f_oF2 varies from *2 MHz* to *4 MHz* from September to April and from *5 MHz* to *6 MHz* from April to September. Closer examination of each panel reveals three distinct features: the first is an enhancement in electron density observed at dusk at about *19:00–20:00 LT* and appears from April till September; the second is a reduction in electron density in the morning around *07:00 LT* in all months except September and March. It is predominantly visible in October. The third feature is the fluctuations seen from May till the end of August.

Fig. 5 illustrates the monthly averaged diurnal peak height variations (h_mF2). The figure was created the same way as Fig. 4. Features seen in the single day plot of Fig. 4 are also visible in these average plots for each month. Figure displays clearly that the ionosphere is lower during day than at night throughout the year, as expected from the theory. The noon peak height is more than 50% lower than midnight peak height in all months varying approximately from *210 km* to *400 km.* While the noon peak height h_mF2 is well pronounced from October till June, it flattens out from June till October. Especially, the appearance of the peak at noon time in October, which is sharply defined, and June, which is rather flat, presents a striking comparison. Also, the noon h_mF2 is the lowest in winter months compared to those in other months. The relative change between noon and midnight h_mF2 is seen smaller in May and summer months than in winter months, mainly because of the rise of the ionosphere at dawn and dusk. In addition, the h_mF2 shows two minima at about *09:00 LT* around dawn and about *18:00 LT* around dusk throughout the year. The minimum values of h_mF2 at dawn and dusk differ in each month. Except November and July, h_mF2 at dawn sector is seen to be smaller than that at dusk sector for all months. Daytime h_mF2 in summer months remains almost constant at about *260 km* on the average. A sharp decrease of h_mF2 at about *05:30 LT* in November corresponds to the sharp decrease seen in f_oF2 plots in Fig. 4.

Fig. 6 presents and compares the monthly averaged diurnal *TEC*. The figure was created in the same way as in Figs. 4 and 5. The figure displays that the spring months have the largest *TEC* at both local noon and midnight whereas the winter months show the smallest *TEC*. The noon *TEC* indicates a maximum at *26.5 TECU* in May and a minimum at *12.5 TECU* in February. Similarly, the midnight *TEC* is maximum at *7.5 TECU* in May and min-

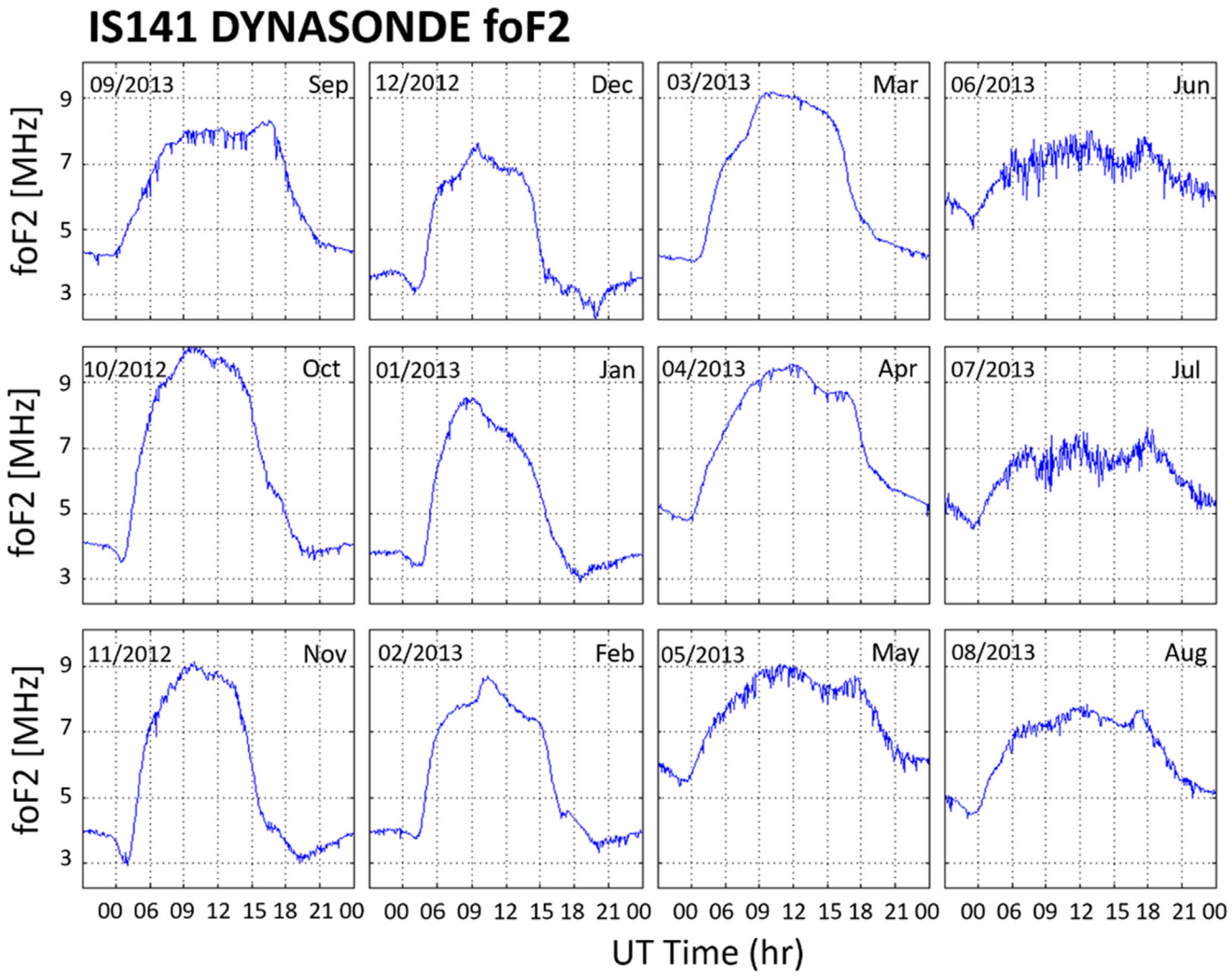

Fig. 4. Monthly averaged diurnal variations of critical frequency (f_oF2). Note that the vertical scale in each panel starts at *2 MHz*.

imum at *1.5 TECU* in December. The *TEC* in winter and summer months exhibits a rather symmetric diurnal variation around the peak, tracking the diurnal variations in the solar zenith angle. However, in March, April and May, it is seen to increase faster before the peak and decline slower after the peak while the opposite is seen in September, October and November, meaning it rises gradually before and drops quickly after the peak. The noon peak in *TEC* occurs slightly earlier than that of f_oF2 in all months, but especially in summer months. The time difference between the peaks of f_oF2 and the *TEC* is about *40* min on average in summer months while it is reduced in winter months. The largest time difference between the peaks occurs in June when the peak *TEC* is seen about *2 hrs* earlier than that of f_oF2.

In addition, Fig. 6 illustrates that the TEC fluctuates throughout the year, with relatively high fluctuations from May through the end of August. The largest fluctuations are dominantly found in May, June and July and can exist any time of the day while they are constrained primarily around noon time with smaller amplitudes in other months, but especially winter. The investigation of single day *TEC* variations in summer months indicates that the fluctuations are present almost every day during the summer months and can be seen several times in a day with different durations. While monthly averaging of *TEC* in Fig. 6 removes some of the weaker fluctuations, the fluctuations remained point at the ionospheric dynamics playing role on the electron density profile in winter and summer months as well as during the daytime and night time.

Fig. 7 presents the seasonally averaged diurnal variations of f_oF2, h_mF2 and the *TEC*. The figure was created by taking the averages at every *4* min over the three months of each season. Thus, the figure illustrates and compares average diurnal variations for each season. In the figure, the columns display f_oF2, h_mF2 and the *TEC* from left to right while the rows indicate the seasons from top to bottom as fall, winter, spring and summer. The most striking differences are seen in summer season. The summer variations of all three parameters are characterized by strong fluctuations, and flattened noontime variations. In addition to these, the figure shows two clear, prominent seasonal

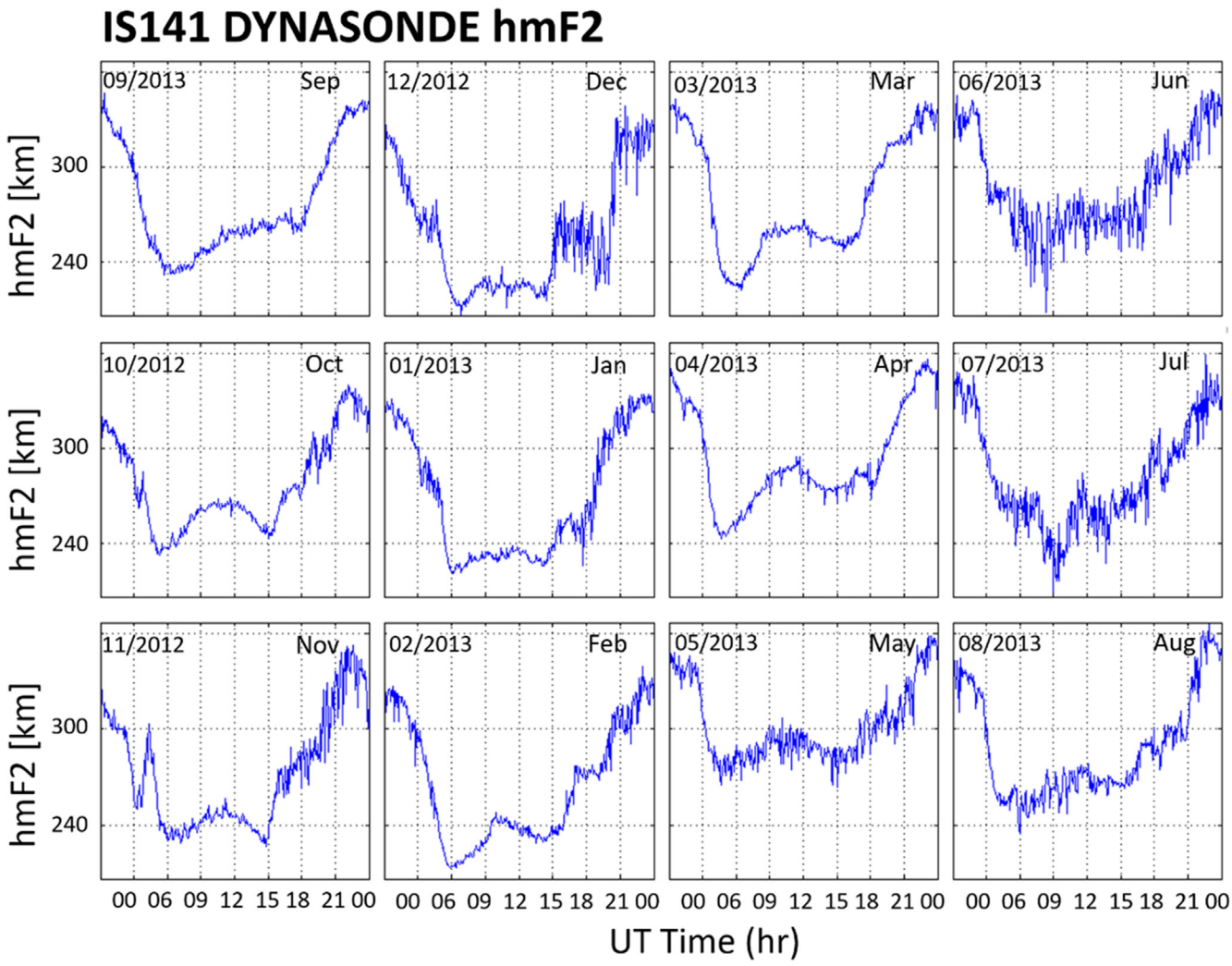

Fig. 5. Monthly averaged diurnal variations of peak height (h_mF2). Note that the vertical scale in each panel starts at *210 km*.

features in f_oF2: one is an enhancement around dusk and the other is a reduction at dawn. While the dusk increase at about *20:00 LT* is a clear summertime feature for both f_oF2 and *TEC*, dawn reduction is seen as a characteristic of all seasons in f_oF2 but not as definite in *TEC*. Local time of the dawn depression of f_oF2 differs between the seasons. It occurs around *06:30 LT* in spring and summer, and around *08:00 LT* in fall and winter. All three parameters, f_oF2, h_mF2, and the *TEC* attain the lowest/highest values during summer daytime/nighttime when compared to fall, winter and spring values. Diurnal distribution of both f_oF2 and the *TEC* agrees with solar zenith angle variations during the day in fall, winter and spring. In summer, on the other hand, the f_oF2 during the daytime cannot described by the solar variations.

3.2. On the existence of ionospheric anomalies

As a further step, in this part, we look at the existence of the ionospheric anomalies over this region. For this purpose, we used median statistics of f_oF2 to assign the presence of an anomaly. Fig. 8 presents median f_oF2 at noon (*12:00 LT*) and midnight (*24:00 LT*) according to months (top) and seasons (bottom). In the panels, noontime f_oF2 is plotted in light gray while midnight f_oF2 is shown in dark gray. We made similar plots using mean noon and midnight critical frequency as well. Here, we present results from median as it is the most commonly used one in the literature but note that the mean critical frequency (Table 1) gives the similar results. Both the top and bottom panels clearly demonstrate that the semiannual anomaly is the main feature of the noon f_oF2. In contrast, the winter anomaly does not appear to be present. Comparing the critical frequency in December (7.12 MHz) with the critical frequency in June (7.91 MHz) indicate the electron densities are smaller in December than in June. The use of January and July for winter and summer, (i.e. critical frequencies *8.03 MHz* versus *7.15 MHz*), indicates the presence of winter anomaly. Rishbeth and Mendillo (2001) used January and July to search for the existence of annual anomaly using worldwide ionospheric data noting that it would not make a big change using them instead of

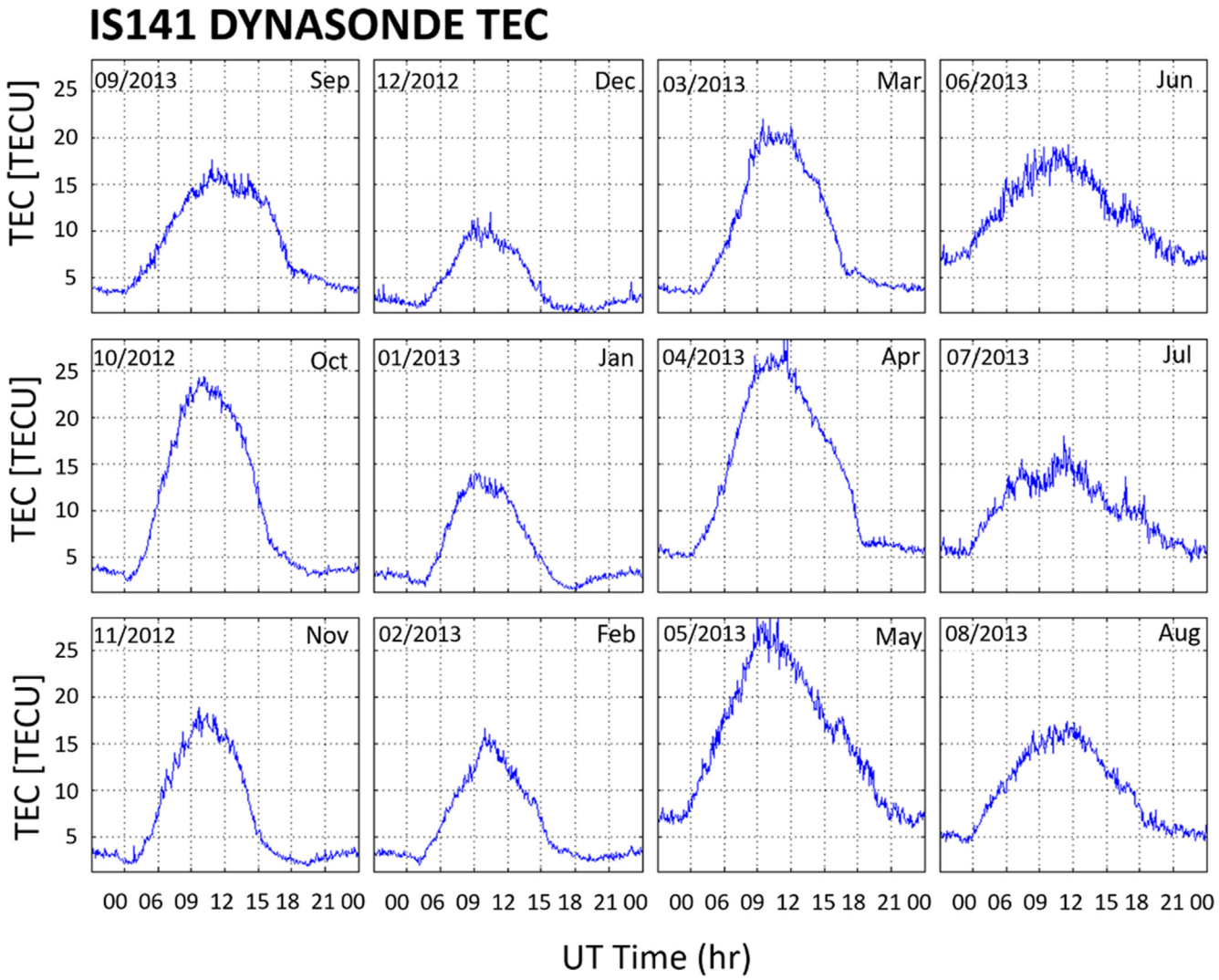

Fig. 6. Monthly averaged diurnal variations of Total Electron Content (*TEC*).

December and June for their study. In any case, it can be seen that the winter anomaly would be a weaker feature compared to semi-annual anomaly, despite that the winter, as a whole season, in Panel *b* shows higher electron densities at noon time than the summer. Table 1 summarizes the presence of anomalies over this region. In the table, median critical frequencies at noon in winter (December) and summer (June) are compared for the presence of winter anomaly, while the noon time critical frequencies for equinox and solstice are compared for the presence of semi-annual anomaly. For equinox, average of median critical frequencies at noon in March and September, and for solstice, average of median critical frequencies at noon in December and June were used.

3.3. Classification of daily f_oF2 variations

In this part, we examined diurnal variations closer. We extended our search from October *2012* to November *2014* and visually scanned the daily time series plots of f_oF2. This search involves scanning of about *750* ionograms in about two years (*25* months). We categorized the diurnal variations of f_oF2 presented in Fig. 4. During the scanning, special features are recorded and at the end of the scanning process, diurnal variations with similar features were grouped into Types. While this categorization will expose the most typical diurnal variations, it will also help to identify the dynamical mechanisms that affect the electron density variations over mid-latitudes. As a result of this inspection, we have identified four types of diurnal variations. While some of the features that define the Types are also apparent in the average plots of Figs. 4, 5, 6 and 7, some are visible only in the single day plots which are not averaged, and thus suggesting different time scales for their occurrence. Fig. 9 summarizes the results of this search that categorizes the patterns detected in f_oF2 diurnal variations as Type *1*, Type *2*, Type *3* and Type *4*. Type *1* shows a variation consistent with the Chapman theory. In other words, Type 1 electron density is maximum at noon and minimum at midnight following the variations in the solar zenith

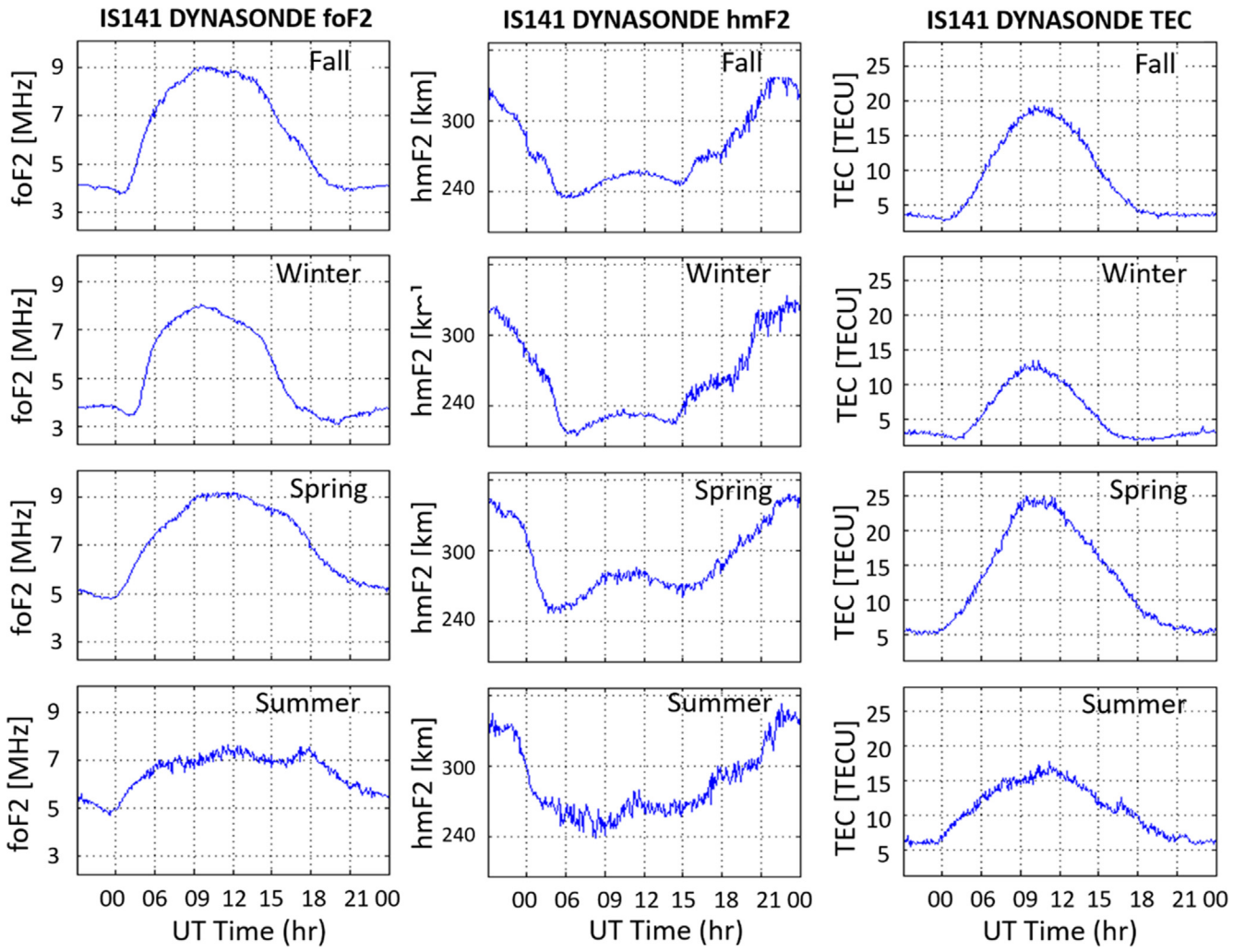

Fig. 7. Seasonally averaged diurnal variations of f_oF2 (left), h_mF2 (middle) and *TEC* (right).

angle. Type *1* represents the fundamental diurnal variation of f_oF2 and all other Types can be described as deviations with respect to Type *1*. Type *2* exhibits a depression instead of a peak at noon. Type *3* displays a bulge in the afternoon, usually at dusk, about *17:30 LT* as in this example. The last type, Type *4*, exhibits wave-like features that appear any time of the day. In this example, the wave-like fluctuations exist from about *20:00 LT* to *00:00 LT*. Our search indicates that these fluctuations occur most of the time around sunset or just after the sunset in the evening, but not restricted to.

Fig. 10 gives the annual distribution of the occurrence rates for each Type. Panels on the left from top to bottom present Type *1*, Type *2*, Type *3*, and Type *4* respectively. Vertical axis is the monthly occurrence rate in percentage obtained by dividing the total number of occurrences of a particular Type to the total number of diurnal plots of f_oF2 in each month. Horizontal axis shows the months starting with December. In these panels, we see that the occurrence rate of Type *1* is maximum in April and minimum in July with a rate of *75%* and *6%* respectively. Occurrence rate of Type *2*, on the other hand, is maximum in January (*61%*) and minimum in April (*15%*). Type *3* shows a maximum rate of occurrence in July with *70%* and a minimum in April and January with a rate of *10%*. Last panel on the left exhibits that the Type *4* is the most frequently seen Type with a maximum occurrence rate in June and July (*100%*) and a minimum in December (*36%*). Its occurrence rate increases from March to October varying around *95%*, and around 54% on average in other months. We note that the occurrence rate of *100%* for a specific Type does not mean that other Types do not occur. For example, Type *3* has its maximum occurrence in July as well, but its occurrence rate is smaller, about *70%,* when compared to that of Type 4 in this month. Annual occurrence rates based on these panels on the left are found as *39%*, *27%*, *34%,* and *84%* for Type *1*, Type *2*, Type *3* and Type *4* respectively.

In our visual search, Type *1* and Type *2* are identified as the only pure types that exist alone. Type *3*, on the other hand, is a feature superimposed on either Type *1* or Type *2*. Those Type *1* and Type *2* with Type *3* feature on are

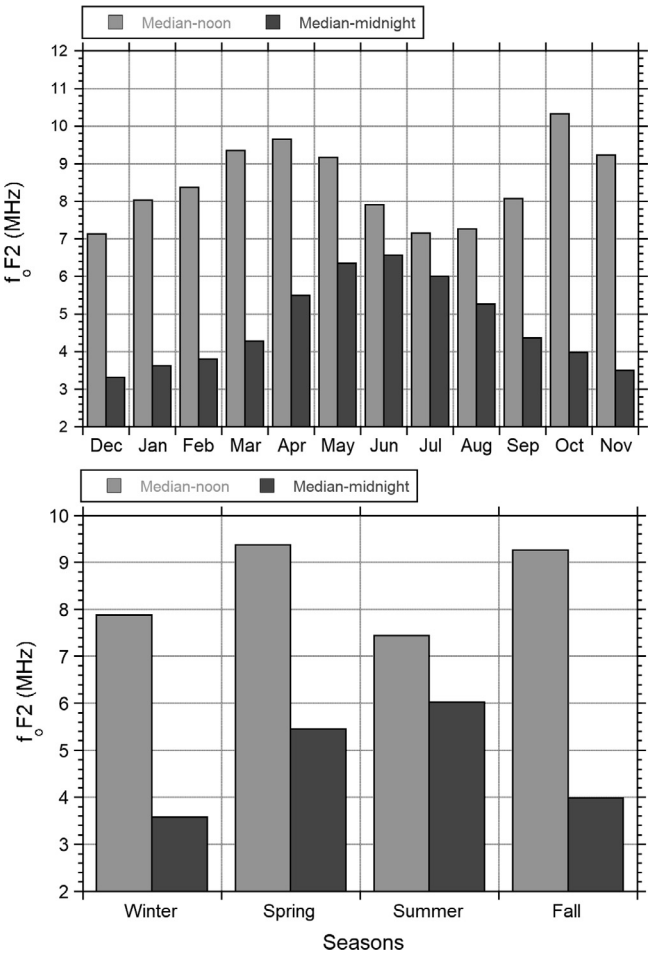

Fig. 8. (top) Monthly and (bottom) seasonal variation of noon (light gray) and midnight (dark gray) median f_oF2. Note that the scale on the vertical axes starts at *2 MHz*.

not taken into account in the occurrence rates of Type *1* and Type *2* given on the left panels of Fig. 10. That is, occurrence of Type *3* comprises some Type *1* and some Type *2* by the nature of its definition. Therefore, the decrease of Type *1* and Type 2 in summer months seen in the top left panels of Fig. 10, for example, is partially due to an increase in Type *3*. Similar to Type *3*, Type *4* is a superimposed feature as well and is identified regardless of the presence of Type *1*, Type *2*, and Type *3*. Its occurrence rate is determined on yes-or-no basis during the visual scans. The top two panels on the right in Fig. 10 display the occurrence rates of Type *1* and Type *2* without a separation for Type *3*. Even though some increase in the occurrence rates of Type *1* and Type *2* are seen in all months, the highest contribution from Type *3* presence is found in summer months when Type *3* is seen to be the highest. In this case, Type *1* indicates a maximum increase in August by about *33%* and Type *2* shows an increase maximum in June by about *36%*. Between Type *1* and Type *2*, the more increase occurred in Type *2* in summer months, *10%* versus *24%* on average. This indicates Type *3* accompanies Type *2* more compared to Type *1* in summer months. Examining the top panel on the right, we see that the occurrence rate of Type *1* is still the smallest in July and largest in April. We can also see that Type *2* occurrence is increased in December and February substantially. The bottom two panels on the right in Fig. 10 are the same panels as on the left used only to close the space in the figure.

Table 2 below presents the annual occurrence rates for all types in detail. In the Table, reading first rows then columns, for example, Type *1* versus Type *3* means that Type *3* feature is superimposed on Type *1* and the occurrence rate is *56%*. Similarly, Type *3* versus Type *1* should be interpreted as the amount of Type *1* within Type *3*. Its appearance per year amounts to *16%*. As the Table indicates the occurrence rates of Type *1* and Type *2* are higher if those occur together with Type *3* is included. Table also indicates that the partitioning between Type *1* and Type *2* within Type *3* is equally distributed in a year by an amount of *17%*. The annual occurrence rates of these Type *1* and Type *2* when Type *3* is included vary around *56%* and *44%*, respectively.

4. Discussion

Categorization of the diurnal variations in electron density using f_oF2 is a new contribution to demonstrate the diurnal variations in the ionosphere over our latitudes. The presence of the types implies the different mechanisms that cause them and indicate highly dynamic ionosphere over our latitudes. Each Type indicates a diurnal variation in the electron density that may result from the solar zenith angle variations, solar and magnetospheric activity, thermospheric neutral winds and compositional changes, meteorological variations from the lower atmosphere, or any combination of these factors depending on the latitude and time (e.g. Rishbeth and Mendillo, 2001; Zou et al., 2000; Forbes et al., 2000). Except Type *4*, which exists all

Table 1
Summary of the ionospheric anomalies based on *F*-region critical frequency over İstanbul. Anomalies are referred on the base of f_oF2 as it is associated with the electron density.

Anomaly	Definition for presence	Mean f_oF2 (*MHz*)	Median f_oF2 (*MHz*)	Exist (?)
Winter (Seasonal or Solstical)	Winter > Summer (Dec-noon > June-noon)	7.21 < 7.58	7.12 < 7.91	NO
Semi-Annual (Equinoctial)	Equinox > Solstice Noon averages (Mar + Sep) > (Dec + Jun)	8.63 > 7.40	8.72 > 7.52	YES

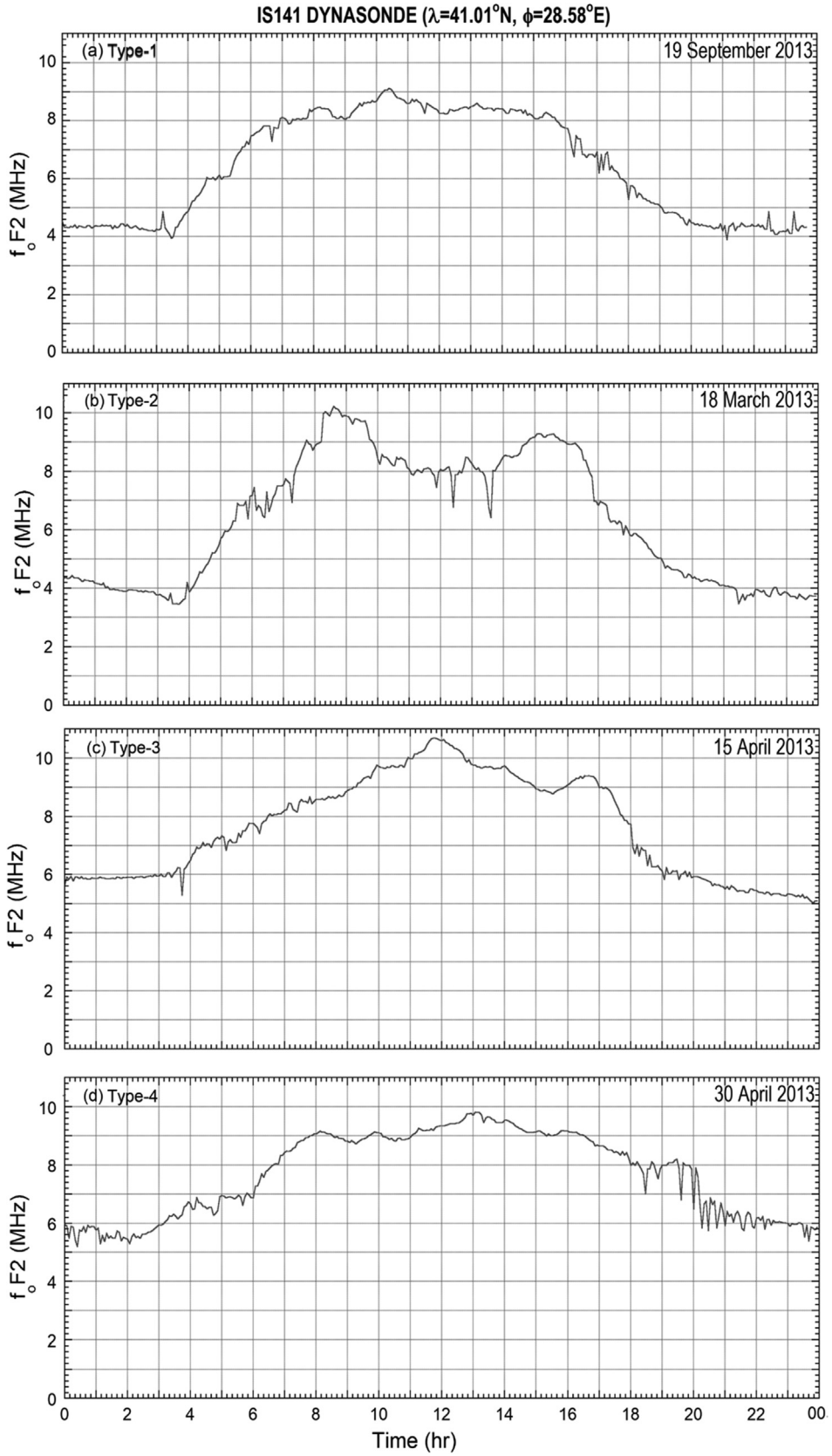

Fig. 9. Categorization of the diurnal variations of f_oF2 into Types: (a) Type *1*, (b) Type *2*, (c) Type *3*, (d) Type *4*.

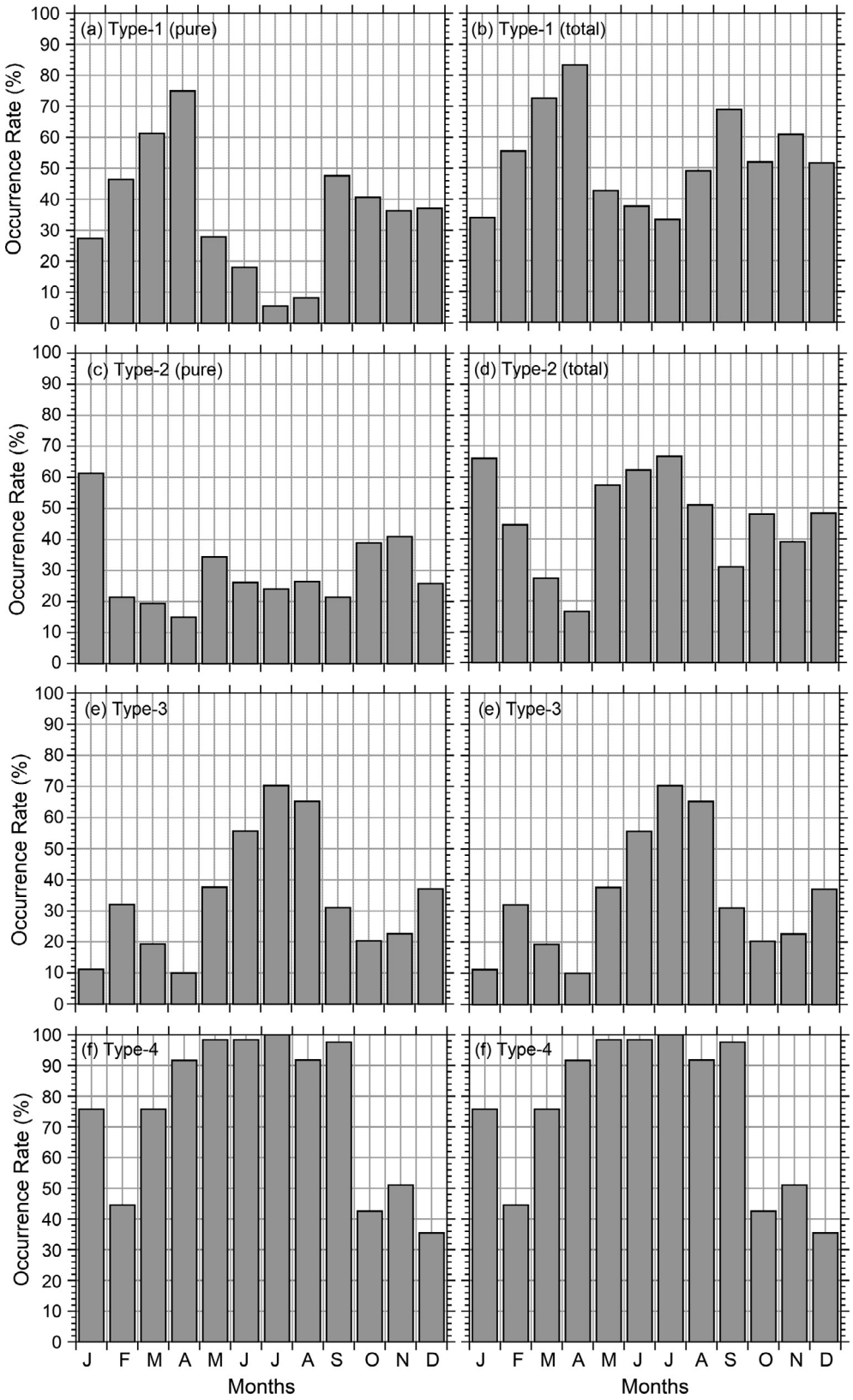

Fig. 10. Monthly distribution of Types. From top to bottom: the first column presents Type *1* (pure), Type *2* (pure), Type *3*, Type *4* and the second column gives Type *1* (total), Type *2* (total). Type *3* and Type *4* on the second column are repeated to fill the space.

year around, it is demonstrated that Type *1* occurrence is the highest (pure *39%*) during a year. Especially in spring and fall, Type *1* dominates over Type *2* and Type *3*. Type *1* illustrates the most basic and the typical diurnal variation of the electron density during a day and identifies the source as the variations in the solar zenith angle. This type

Table 2
Annual occurrence rates of ionospheric Types.

Annual rates, %	Type *1*	Type *2*	Type *3*	Type *4*
Type *1*	39	0	56	16, No wave-like feature
Type *2*	0	27	44	
Type *3*	17	18	34	
Type *4*	16, No wave-like feature			84

of diurnal variation of electron density was well-established at different latitudes over the world (Kim and Hegai, 2009; Medvedev and Tolstikov, 2015; Zou et al., 2000; Wright, 1962). It was also reported widely that the diurnal electron density variations do not agree with the Chapman theory (e.g. Wright, 1962). Our study also indicates that diurnal variation of electron density away from the Chapman theory is a common feature over our station. This is most obvious in summer when Type *1* occurrence rate reduces while Type *2* and Type *3* occurrences enhance. It is also clear that the monthly averaged diurnal variations of f_oF2, h_mF2 and *TEC* presented in Figs. 4, 5, 6, 7 do not support Chapman theory in summer. Type 2 (pure 29%) is the second most common type of diurnal electron density variation seen in our region. Both Type *2* and Type *3* were found to be the highest in summer as opposed to Type *1*. The summer enhancements in Type *2* and Type *3* and summer reduction in Type *1* indicate other sources affecting the diurnal electron distribution over this region, in addition to the solar zenith angle variations. These may be attributed to the thermospheric neutral winds that move the electrons along the magnetic field lines out of F-region heights as suggested in several earlier studies (Zou et al., 2000; Rishbeth and Müller-Wodarg, 1999; Rishbeth, 1998; Fuller-Rowell et al., 1994, 1996).

The magnetospheric activities are suggested to reduce or enhance the electron density as well. As reviewed in Mendillo (2006), and Prölss (1995), the *TEC* shows an increase and decrease with respect to a quiet day electron density variation. These are called as the positive and negative phases of an ionospheric storm and observed most commonly at subauroral latitudes as a result of the increased auroral energy released from the magnetotail during the substorms. Both Type *2* and Type *3* have features similar to those of negative and positive signatures seen in *TEC*'s response to geomagnetic activity (Mendillo, 2006; Rishbeth and Mendillo, 2001). The features such as noon depression and dusk bulge, that construct Type 2 and Type 3, were also found in the electron density data from Slough (52^oN) station as associated with the geomagnetic activity (Rishbeth and Mendillo, 2001). The time period of our study corresponds to the peak of the solar activity cycle which indicates more magnetospheric activity as well. Although İstanbul (40^oN) is away from the auroral latitudes, the observation of the similar diurnal characteristics indicates the possible effects of the high latitude phenomena that may extend toward mid-latitudes, especially during the periods of high solar activity and modify the mid-latitude electron density. The more occurrence rate of Type *2* and Type *3* in summer compared to winter may be associated with magnetospheric, and/or solar activity (Russell and McPherron, 1973; Torr and Torr, 1973). For example, the day that Type *2* in Fig. 8 was observed corresponds to a strong geomagnetic storm ($D_{st} \leq$ *-100 nT*) which seems to give rise to the depression seen in the electron density at noon time (Mendillo, 2006; Gonzalez et al., 1994). While whether all the depressions at noon time is a result of geomagnetic activity is a subject of further research, to address this point, as a straight forward approach, we plotted the number of days when the auroral electrojet index (*AE*) exceeds *500 nT*, that corresponds to moderate to strong auroral activity levels, from Oct. *2012* to Sep. *2013*. Fig. 11 is constructed to compare the monthly occurrence rates of Types with the auroral activity as determined by *AE*. In the figure, vertical axes on the right and left are the number of geomagnetically active days and the occurrence rate of Types respectively. Type *1* and Type *2* in this figure are plotted both as pure (blue line with triangles) and total (red line with squares), namely with and without Type 3 as given on the top two panels in Fig. 10. Magnetospheric substorms occur in the magnetotail as a consequence of near-Earth magnetic reconnection and result in auroral particle precipitation and auroral energy flow into the ionospheric heights at especially high latitudes above *60°*. Auroral Electrojet (*AE*) index based on the auroral activity level is used to identify the magnetospheric substorms and commonly *AE > 100 nT* indicates occurrence of a substorm. Examination of these panels in Fig. 11 indicates that the reduction in Type *1* and increasing rates of Type *2* and Type *3* in summer, starting from month of April till September, are closely associated with the number of geomagnetically active days. Type *3* is seen to be a feature produced by the geomagnetic effects as its occurrence is consistent with the monthly distribution of the geomagnetically active days very well. That is, it is high in summer when activity days are high and low in winter when activity days are low. Low occurrence rates of Types *1* in winter and fall are also consistent with the low number of activity days. Type *2*, on the other hand, is high in winter corresponding to less activity. This will imply a cause that operates in winter to produce Type *2* but reduce Type *1* and Type *3*. Similar to Type *3*, Type *4* appears to follow the variations in the geomagnetic activity days in general as well. This quick search on the possible relation between the geomagnetically active days and occurrence rate of Types indicate clearly

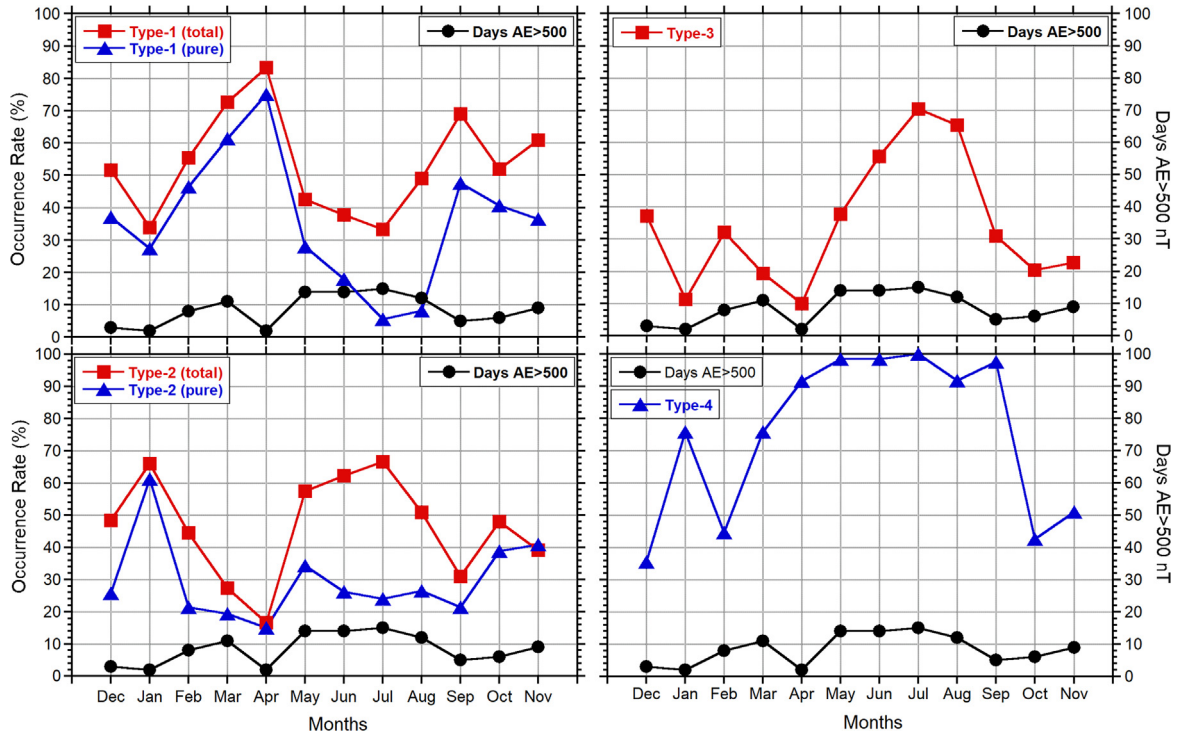

Fig. 11. The occurrence rate of Types are compared with the auroral activity days when $AE > 500\ nT$. Right axis gives the days with AE > 500 nT for all panels. (For interpretation of the references to color in this figure legend, the reader is referred to the web version of this article.).

that the solar zenith angle is not the only factor that determine the electron density variations. Part of the differences in the occurrence rates of Types, especially in winter and summer months can be attributed to the geomagnetic effects on the electron density variation. Therefore, it is suggested that the effects of geomagnetic activity should be taken into account in addition to other factors such as solar zenith angle, atmospheric waves, the neutral winds, change in the neutral composition of the upper atmosphere (Mendillo et al., 2002; Rishbeth and Mendillo, 2001; Zou et al., 2000; Rishbeth, 1998; Rishbeth and Müller-Wodarg, 1999; Fuller-Rowell and Rees, 1983) when studying the causes of electron density variations over this region.

In addition to Types, we have shown that the fluctuation levels in critical frequency (f_oF2), and thus electron density, are higher in summer than in winter. High fluctuation levels in summer can be seen as associated with the high number of geomagnetically active days in summer as presented in Fig. 11. Similarly, the high electron density at midnight in summer months compared to those in winter is found to be related to the increased number of geomagnetically active days in summer. We have also shown that the winter electron density is higher than summer electron density at noon and it is the opposite at midnight. Although our data in December and June do not support the presence of winter anomaly, comparison of the electron densities in January and July at noon, or the winter season and summer season at noon, indicates its presence. The difference between winter and summer median critical frequencies in Fig. 9 is not large, only about *10%*. Depending on the latitude and the amount of solar radiation flux and solar/geomagnetic activity levels, one or more of the anomalies may become dominant at different magnitudes at different times of the year. It is reported that while the winter anomaly is more common feature observed at higher latitudes, semi-annual anomaly is seen more often at low latitudes (Zou et al., 2000; Yasyukevich et al., 2018; Rishbeth and Müller-Wodarg, 1999; Wright, 1962). The winter anomaly was found to be weaker at mid-latitudes and reported as about *15%* in Zou et al. (2000). Investigation of seasonal patterns in Irkutsk (*52°*) Digisonde data shows no winter anomaly as well. The authors attribute its absence to the dependence of the effect on the geomagnetic latitude and consequently being "far-from-pole" feature of their site (Ratovsky and Oinats, 2011). The strength of the winter anomaly, on the other hand, was shown to be sensitive to solar and geomagnetic activity (Yasyukevich et al., 2018; Lee et al., 2011; Park et al. 2010; Pavlov and Pavlova, 2005; Zou et al., 2000). In addition to the geomagnetic and solar activity effects at mid-latitudes, occurrence of winter anomaly is also shown to be associated with the seasonal changes in the chemical composition of the thermospheric neutral air (Rishbeth and Mendillo, 2001; Rishbeth, 2006; Rishbeth, 1998; Fuller-Rowell and Rees, 1983; Duncan, 1956; Wright, 1962; Rishbeth and Setty, 1961) as well as the Travelling Ionospheric Disturbances (*TIDs*) (Ratovsky et al., 2015). Considering these

previous studies, one or more of these factors can contribute on the existence and magnitude of the winter anomaly at our station.

In contrast to winter anomaly, the semi-annual anomaly is found to be a more pronounced feature seen over our region. It was reported to exist in some regions as strong as *20%* (Rishbeth and Mendillo, 2001) at subauroral latitude stations while it was found to be less pronounced (Park et al., 2010) or it is not existed in some other locations (Millward et al. 1996), especially during the low solar activity. The presence of semi-annual anomaly is generally attributed to semiannual variations in neutral density (Fuller-Rowell, 1998; Rishbeth and Müller-Wodarg, 1999) and geomagnetic activity (Waltersheid, 1982). In Fig. 11, we see that number of geomagnetically active days are almost equal in equinox and solstice months which indicates a lower possibility of geomagnetic activity on the existence of semiannual-anomaly. Therefore, other factors may be more dominant such as semi-annual variation of thermospheric neutral density and/or atmospheric waves for its presence in our station.

5. Conclusions

In this paper, we presented first observations from ITU-Dynasonde in order to show typical characteristics of the ionosphere over Istanbul. Ionospheric f_oF2, h_mF2, the *TEC* data and ionograms with *4* min resolution were used for the analysis. While the results from this study support the findings of the earlier studies at mid-latitudes, some of the features were newly demonstrated for our region. Among these are the summer/winter differences in f_oF2, h_mF2 and *TEC*, fluctuation levels, presence/absence of ionospheric anomalies. In addition, we have categorized the diurnal variations of f_oF2 into classes called as Types. The diurnal, monthly and seasonal variations we presented in all ionospheric parameters and the existence of Types suggest different physical mechanisms that operate at different times of the year. These can be changes in the thermospheric composition such as the oxygen-to-nitrogen ratio, thermospheric neutral winds, and geomagnetic and solar cycle variations. We also presented the close association of the Types with the geomagnetic activity which appears to be one of the causal mechanisms that should be considered in the diurnal variations of electron density in our region. Several of these mechanisms might operate at the same time to account for the electron density variations we observed in our data. However, a distinction between different sources and their contribution on the occurrence of the anomalies or on the occurrence of each Type is not possible at this time and requires a detailed analysis which we consider as a future work.

Ionospheric electron density and its variations are crucial parameters in determination of the communication characteristics of a region which are used in several key sectors such as military and radar technologies. Our observations are unique to this region and this is the first time a detailed investigation of ionospheric parameters conducted using Dynasonde measurements. While this study will help us to develop a local empirical model of electron density variability over our latitudes, we anticipate that they will also contribute in the efforts of the global ionospheric space weather modelling studies.

Declaration of Competing Interest

The authors declare that they have no known competing financial interests or personal relationships that could have appeared to influence the work reported in this paper.

Acknowledgment

This work has been supported by TÜBİTAK 113Y213. It was also partially supported by Research Program (BAP) of Istanbul Technical University (ITU), No=36514. We would like to acknowledge the ITU-Rectorate for their support while establishing the Dynasonde system in ITU campus and for its maintenance. Also we would like to thank Dr. Filiz Türk Katırcıoğlu and Dr. Terry Bullet for their help and encouragement during the initial stages of the installation of the system within the campus. This work was also partially supported by NSF, USA grant 1643119.

References

Borries, C., Jakowski, N., Wilken, V., 2009. Storm induced large scale TIDs observed in GPS derived TEC. Ann. Geophys. 27 (4), 1605–1612. https://doi.org/10.5194/angeo-27-1605-2009.

Bruinsma, S.L., Forbes, J.M., 2007. Global observation of traveling atmospheric disturbances (TADs) in the thermosphere. Geophys. Res. Lett. 34, L14103. https://doi.org/10.1029/2007GL030243.

Cherniak, I., Zakharenlova, I., 2018. Large-scale traveling ionospheric disturbances origin and propagation: Case study of the December 2015geomagnetic storm. Space Weather 16, 1377–1395. https://doi.org/10.1029/2018SW001869.

Duncan, R.A., 1956. The behavior of a Chapman layer in the night F2 region of the ionosphere, under the influence of gravity, diffusion, and attachment. Aust. J. Phys. 9, 436–439. https://doi.org/10.1071/PH560436.

Forbes, J.M., Palo, S.E., Zhang, X., 2000. Variability of the ionosphere. J. Atmos. Sol. Terr. Phys. 62, 685–693. https://doi.org/10.1016/S1364-6826(97)82016-0.

Francis, S.H., 1974. A theory of medium-scale traveling ionospheric disturbances. J. Geophys. Res. 79 (34), 5245–5260. https://doi.org/10.1029/JA079i034p05245.

Fuller-Rowell, T.J., Codrescu, M.V., Wilkinson, P., 2000. Quantitative modelling of the ionospheric response to geomagnetic activity. Ann. Geophys. 18, 766–778. https://doi.org/10.1007/s005850000233.

Fuller-Rowell, T.J., 1998. The 'thermospheric spoon': a mechanism for the semi-annual density variation. J. Geophys. Res. 103, 3951–3959. https://doi.org/10.1029/97JA03335.

Fuller-Rowell, T.J., Codrescu, M.V., Rishbeth, H., Moffett, R.J., Quegan, S., 1996. On the seasonal response of the thermosphere and ionosphere to geomagnetic storms. J. Geophys. Res. 101, 2343–2353. https://doi.org/10.1029/95JA01614.

Fuller-Rowell, T.J., Codrescu, M.V., Moffett, R.J., Quegan, S., 1994. Response of the thermosphere and ionosphere to geomagnetic storms. J. Geophys. Res. 99, 3893–3914. https://doi.org/10.1029/93JA02015.

Fuller-Rowell, T.J., Rees, D., 1983. Derivation of a conservative equation for mean molecular weight for a two constituent gas within a three-dimensional, time-dependent model of the thermosphere. Planet. Space Sci. 31, 1209–1222. https://doi.org/10.1016/0032-0633(83)90112-5.

Gonzalez, W.D., Joselyn, J.A., Kamide, Y., Kroehl, H.W., Rostoker, G., Tsurutani, B.T., Vasyliunas, V.M., 1994. What is a geomagnetic storm?. J. Geophys. Res. 99 (A4), 5771–5792. https://doi.org/10.1029/93JA02867.

Ham, Y.-B., Jee, G., Lee, C., Kwon, H.-J., Kim, J.-H., Zabotin, N., Bullett, T., 2000. Observations of the Polar Ionosphere by the Vertical Incidence Pulsed Ionospheric Radar at Jang Bogo Station, Antarctica. J. Astronomy Space Sci. 37 (2), 143–156. https://doi.org/10.5140/JASS.2020.37.2.143.

Heaton, J.A.T., JoNEs, G.O.L., Kersley, L., 1996. Toward ionospheric tomography in Antarctica: first steps and comparison with dynasonde observations. Antarctic Sci. 8, 297–303. DOI: 10.1017/S0954102096000430.

Hernández-Pajares, M., Juan, J.M., Sanz, J., 2006. Medium-scale traveling ionospheric disturbances affecting GPS measurements: Spatial and temporal analysis. J. Geophys. Res. 111, A7, A07S11. https://doi.org/10.1029/2005JA011474.

Hsiao, T.Y., Tsai, L.-C., Berkey, F.T., 2008. The initial results of the Chung-Li Dynasonde for RF environment surveillance and ionospheric observations. Terrestrial Atmos. Oceanic Sci. 19 (5), 515–524. https://doi.org/10.3319/TAO.2008.19.5.515(AA).

Kim, J.-E., Kim, J.-H., Jee, G., Lee, C., Kwon, H.-J., Ham, Y.-B., Bullett, T., Wu, Q., Mabie, J., Nikolay, Z., 2018. Ground-based observations for the upper atmosphere at Jang Bogo Station, Antarctica: preliminary results. Curr. Sci. 115 (9), 1674–1678. https://doi.org/10.18520/cs/v115/i9/1674-1678.

Kim, V.P., Hegai, V.V., 2009. On the variability of the ionospheric F2-layer during the quietest days in December 2009. J. Astron. Space Sci. 33 (4), 273–278. https://doi.org/10.5140/JASS.2016.33.4.273.

Kirchengast, G., 1997. Characteristics of high-latitude TIDs from different causative mechanisms deduced by theoretical modeling. J. Geophys. Res. 102 (A3), 4597–4612. https://doi.org/10.1029/96JA03294.

Lal, C., 1998. Solar wind and equinoctial maxima in geophysical phenomena. J. Atmos. Terrestrial Phys. 60, 1017–1024. https://doi.org/10.1016/S1364-6826(98)00046-7.

Lal, C., 1992. Global F2 layer ionization and geomagnetic activity. J. Geophys. Res. 97, 12153–12159. https://doi.org/10.1029/92JA00325.

Lee, W.K., Kil, H., Kwak, Y.-.-S., Wu, Q., Cho, S., Park, J.U., 2011. The winter anomaly in the middle-latitude F region during solar minimum period observed by the Constellation Observing System for Meteorology, Ionosphere, and Climate. J. Geophys. Res. 116, A02302. https://doi.org/10.1029/2010JA015815.

Liu, J.-Y., Pan, C.-J., Lee, C.-C., 2002. VHF radar and MF/HF Dynasonde observations during Polar Mesosphere Summer Echoes conditions at EISCAT. Earth, Planets Space 54, 691–698. https://doi.org/10.1186/BF03351720.

Medvedev, A.V., Tolstikov, M.V., 2015. Diurnal, seasonal and solar activity pattern of ionospheric variability from Irkutsk Digisonde data. Adv. Space Res. 55, 2041–2047. https://doi.org/10.1016/j.asr.2014.08.001.

Mendillo, M., 2006. Storms in the ionosphere: Patterns and processes for total electron content. Rev. Geophys. 44. https://doi.org/10.1029/2005RG000193.

Mendillo, M., Rishbeth, H., Roble, R.G., Wroten, J., 2002. Modelling F2-layer seasonal trends and day-to-day variability driven by coupling with the lower atmosphere. J. Atmos. Sol. Terr. Phys. 64, 1911–1931. https://doi.org/10.1016/S1364-6826(02)00193-1.

Millward, G.H., Rishbeth, H., Fuller-Rowell, T.J., Aylward, A.D., Quegan, S., et al., 1996. Ionospheric F2 layer seasonal and semiannual variations. J. Geophys. Res. 101, 5149–15126. https://doi.org/10.1029/95JA03343.

Negrea, C., Zabotin, N., Bullett, T., 2018. Seasonal Variability of the Midlatitude Traveling Ionospheric Disturbances from Wallops Island, VA, Dynasonde Data: Evidence of a Semiannual Variation. J. Geophys. Res. 123 (6), 5047–5054. https://doi.org/10.1029/2017JA025164.

Negrea, C., Zabotin, N., Bullett, T., Fuller-Rowell, T., Fang, T.-W., et al., 2016. Characteristics of acoustic gravity waves obtained from Dynasonde data. J. Geophys. Res. 121, 3665–3680. https://doi.org/10.1002/2016JA022495.

Park, Y.-K., Kwak, Y.-S., Ahn, B.-H., Park, Y.-D., et al., 2010. Ionospheric F2-layer semi-annual variation in middle latitude by solar activity. J. Astronomy Space Sci. 27 (4), 319–327. https://doi.org/10.5140/JASS.2010.27.4.319.

Pavlov, A.V., Pavlova, N.M., 2005. Causes of the mid-latitude NmF2 winter anomaly at solar maximum. J. Atmos. Terr. Phys. 67, 862–877. https://doi.org/10.1016/j.jastp.2005.02.009.

Prölss, G.W., 2006. Ionospheric F-region storms: unsolved problems. In Characterizing the Ionosphere. Meeting Proceedings RTO-MP-IST-056, Paper 10. Neuilly-sur-Seine, France, pp. 10-1 – 10-20.

Prölss, G.W., 1995. In: Volland, H. (Ed.), Handbook of Atmospheric Electrodynamics, 2. CRC Press, Boca Raton, pp. 195–248. https://doi.org/10.5140/JASS.2010.27.4.319.

Ratovsky, K.G., Medvedev, A.V., Tolstikov, M.V., 2015. Diurnal, seasonal and solar activity pattern of Ionospheric variability from Irkutsk Digisonde data. Adv. Space Res. 55, 2041–2047. https://doi.org/10.1016/j.asr.2014.08.001.

Ratovsky, K.G., Oinats, A.V., 2011. Local empirical model of ionospheric plasma density derived from Digisonde measurements at Irkutsk. Earth Planets Space 63 (4), 351–357. https://doi.org/10.5047/eps.2011.03.002.

Ratovsky, K.G., Oinats, A.V., Medvedev, A.V., 2009. Diurnal and seasonal variations of F2 layer characteristics over Irkutsk during the decrease in solar activity in 2003–2006: Observations and IRI-2001 model predictions. Adv. Space Res. 43, 1806–1811. https://doi.org/10.1016/j.asr.2008.09.029.

Rees, D., 1995. Observations and modelling of ionospheric and thermospheric disturbances during major geomagnetic storms: A review. J. Atmos. Terr. Phys. 57 (12), 1433–1457. https://doi.org/10.1016/0021-9169(94)00142-B.

Reinisch, B.W., Huang, X., 1983. Automatic calculation of electron density profiles from digital ionograms: 3. Processing of bottomside ionograms. Radio Sci. 18 (3), 477–492. https://doi.org/10.1029/RS018i003p00477.

Rietveld, M.T., Wright, J.W., Zaotin, N., Pitteway, 2008. The Tromso dynasonde. Polar Sci. 2 (1), 55–71. https://doi.org/10.1016/j.polar.2008.02.001.

Richmond, A.D., Lu, G., 2000. Upper-atmospheric effects of magnetic storms: A brief tutorial. J. Atmos. Sol. Terr. Phys. 62 (12), 1115–1127. https://doi.org/10.1016/S1364-6826(00)00094-8.

Rishbeth, H., 2006. F-region links with the lower atmosphere?. J. Atmos. Sol. Terr. Phys. 68, 469–478. https://doi.org/10.1016/j.jastp.2005.03.017.

Rishbeth, H., Mendillo, M., 2001. Patterns of F2-layer variability. J. Atmos. Sol. Terr. Phys. 63, 1661–1680. https://doi.org/10.1016/S1364-6826(01)00036-0.

Rishbeth, H., Müller-Wodarg, I.C.F., Zou, L., Fuller-Rowell, T.J., et al., 2000. Annual and semiannual variations in the ionospheric F2-layer: II. Physical discussion. Annales Geophysicae 18, 945–956. https://doi.org/10.1007/s00585-000-0945-6.

Rishbeth, H., Müller-Wodarg, I.F., 1999. Vertical circulation and thermospheric composition: a modelling study. Ann. Geophys. 17, 794–805. https://doi.org/10.1007/s00585-999-0794-x.

Rishbeth, H., 1998. How the thermospheric circulation affects the ionospheric F2 layer. J. Atmos. Terrestrial Phys. 60, 1385–1402. https://doi.org/10.1016/S1364-6826(98)00062-5.

Rishbeth, H., Setty, C.S.G.K., 1961. The *F*-layer at sunrise. J. Atmos. Terr. Phys. 20 (4), 263–276. https://doi.org/10.1016/0021-9169(61)90205-7.

Russell, C.T., McPherron, R.L., 1973. Semiannual variation of geomagnetic activity. J. Geophys. Res. 78, 92–102. https://doi.org/10.1029/JA078i001p00092.

Sedgemore, K.J.F., Williams, P.J.S., Jones, G.O.L., Wright, J.W., 1996. A comparison of EISCAT and dynasonde measurements of the auroral ionosphere. Annales Geophysicae 14, 1403–1412. https://doi.org/10.1007/s00585-996-1403-x.

Sedgemore, K.J.F., Wright, J.W., Williams, P.J.S., Jones, G.O.L, Rietveld, M.T., 1998. Plasma drift estimates from the Dynasonde: comparison with EISCAT observations. Annales Geophysicae 16, 1138–1143. https://doi.org/10.1007/s00585-998-1138-y.

Song, Q., Ding, F., Wan, W., Ning, B., Liu, L., Zhao, B., 2013. Statistical study of large-scale traveling ionospheric disturbances generated by the solar terminator over China. J. Geophys. Res. 118, 4583–4593. https://doi.org/10.1002/jgra.50423.

Titheridge, J.E., 2003a. Model results for the daytime ionospheric E and valley regions. J. Atmos. Solar Terrestrial Phys. 65, 129–137. https://doi.org/10.1016/S1364-6826(02)00231-6.

Titheridge, J.E., 2003b. Ionization below the night F2 layer: A global model. J. Atmos. Solar Terrestrial Phys. 65, 1035–1052. https://doi.org/10.1016/S1364-6826(03)00136-6.

Titheridge, 2001. Production of the low-latitude night E layer. J. Geophys. Res. 106, 781–786, DOI: 10.1029/2000JA900145.

Titheridge, J.E., 2000. Modeling the peak of the ionospheric E-layer. J. Atmos. Solar Terrestrial Phys. 62, 93–111. https://doi.org/10.1016/S1364-6826(99)00102-9.

Titheridge, J.E., 1985. Ionogram analysis with the generalized program POLAN, Report UAG-93, http://www.ips.gov.au/IPSHosted/INAG/uag_93/uag_93.html, World Data Cent. for Solar Terrestrial Physics, Boulder, Colorado, 1985.

Titheridge, J.E., Buonsanto, M.J., 1983. Annual variations in the electron content and height of the F layer in the northern and southern hemispheres, related to neutral compositions. J. Atmospheric and Terrestrial Physics 45, 683–696. https://doi.org/10.1016/S0021-9169(83)80027-0.

Torr, D.G., Richards, P.G., Torr, M.R., 1981. Ionospheric composition: the seasonal anomaly explained. In: The Physical Basis of the Ionosphere in the Solar-Terrestrial System, AGARD Conference Proceedings, N81-23523 14-42, p.15, 1981.

Torr, M.R., Torr, D.G., 1973. The seasonal behavior of the F2-layer of the ionosphere. J. Atmos. Terrestrial Phys. 35, 2237–2251. https://doi.org/10.1016/0021-9169(73)90140-2.

Tsuda, T., Rietveld, M.T., Kosch, M.J., Oyama, S., Hosokawa, K., Nozawa, S., Kawabata, T., Mizuno, A., Ogawa, Y., 2018. Survey of conditions for artificial aurora experiments at EISCAT Tromsø using dynasonde data. Earth Planets Space 70, 40. https://doi.org/10.1186/s40623-018-0805-9.

Tsugawa, T., Otsuka, Y., Coster, A.J., Saito, A., 2007. Medium-scale traveling ionospheric disturbances detected with dense and wide TEC maps over North America. Geophys. Res. Lett. 34, L22101. https://doi.org/10.1029/2007GL031663.

Tsugawa, T., Saito, A., Otsuka, Y., 2004. A statistical study of large-scale traveling ionospheric disturbances using the GPS network in Japan. J. Geophys. Res. 109, A06302. https://doi.org/10.1029/2003JA010302.

Verkhoglyadova, O.P., Tsurutani, B.T., Mannucci1, A.J., Mlynczak, M. G., Hunt, L.A., et al., 2013. Variability of ionospheric TEC during solar and geomagnetic minima (2008 and 2009): external high speed stream drivers. Annales Geophysicae 31, 263–276, DOI: 10.5194/angeo-31-263-2013.

Waltersheid, R.L., 1982. The semiannual oscillation in the thermosphere as a conduction mode. J. Geophys. Res. 87, 10527–10535. https://doi.org/10.1029/JA087iA12p10527.

Wright, J.W., Zabotin, N.A., 2005. The Dynasonde 21 Software Suite: A Solution for System Operation, Maintenance, Data Analysis, Storage and Networking. A booklet published by University of Colorado, 22 pages, 2005.

Wright, J.W., Pitteway, M.L.V., 1999. A new data acquisition concept for digital ionosondes: phase-based echo recognition and real-time parameter estimation. Radio Sci. 34, 871–882. https://doi.org/10.1029/1999RS900039.

Wright, J.W., Pitteway, M.L.V., 1998. Data acquisition and analysis for research ionosondes. In: Computer Aided processing of Ionograms and Ionosonde Records, Proceedings of the XXVth General Assembly of URSI, Lille, France, Aug.28 - Sept. 5, 1996. Ed. by Phil Wilkinson, Report UAG 105, NGDC, NOAA, 325 Broadway, Boulder CO 80303 USA, 1998.

Wright, J.W., 1960a. Comment on models of the ionosphere above h_{max}F2. J. Geophys. Res. 65, 2595–2596. https://doi.org/10.1029/JZ065i009p02595.

Wright, J.W., 1960b. A model of the F region above h_{max}F2. J. Geophys. Res. 65, 185–191. https://doi.org/10.1029/JZ065i001p00185.

Wright, J.W., 1962. Diurnal and seasonal changes in structure of the mid-latitude quiet ionosphere. J. Res. Natl. Bureau Standards-D Radio Propagation 66D (3), 297–312.

Yasyukevich, Y.V., Yasyukevich, A.S., Ratovsky, K.G., Klimenko, M.V., Klimenko, V.V., et al., 2018. Winter anomaly in NmF2 and TEC: when and where it can occur. J. Space Weather Space Climate, 8, A45, DOI:10.1051/swsc/2018036.

Zabotin, N.A., Wright, J.W., Bullett, T.W., Zabotina, L. Ye., 2005. Dynasonde 21 principles of data processing, transmission, storage and web service. Proceedings of the Ionospheric Effects Symposium, (Alexandria, VA, May 5-8, 2005), 7B3-1–7B3-3.

Zabotin, N.A., Wright, J.W., Zhbankov, G.A., 2006. Three-dimensional electron density inversion for Dynasonde ionograms. Radio Sci. 41, RS6S32. https://doi.org/10.1029/2005RS003352.

Zabotin, N., Godin, O.A., Negrea, C., Zabotina, L., 2017. Studies of wave activity in the thermosphere-ionosphere system using Dynasonde techniques, Conference paper, Conference: 2017 XXXIInd General Assembly and Scientific Symposium of the International Union of Radio Science (URSI GASS), Montreal, Canada, 2017, DOI: 10.23919/URSIGASS.2017.8105216.

Zhao, B., Wan, W., Liu, L., Mao, Y., Ren, Z., et al., 2007. Annual and semiannual variations derived from the global maps of ionospheric maps of total electron content. Ann. Geophys. 25, 2513–2526. https://doi.org/10.5194/angeo-25-2513-2007.

Zou, L., Rishbeth, H., Müller-Wodarg, I.C.F., Aylward, A.D., Millward, G.H., et al., 2000. Annual and semiannual variations in the ionospheric F2 layer. I. Modelling. Ann. Geophys. 18, 927–944. https://doi.org/10.1007/s005850050009.